

1 Do Loop Current Eddies stimulate productivity in the Gulf of Mexico?

2

3 Pierre Damien^(1,2), Julio Sheinbaum⁽¹⁾, Orens Pasqueron de Fommervault⁽¹⁾, Julien Jouanno⁽³⁾, Lorena
4 Linacre⁽⁴⁾, Olaf Duteil⁽⁵⁾

5

6 ⁽¹⁾ Departamento de Oceanografía Física, Centro de Investigación Científica y de Educación Superior
7 de, Ensenada, México,

8 ⁽²⁾ University of California, Los Angeles, CA

9 ⁽³⁾ LEGOS, Université de Toulouse, IRD, CNRS, CNES, UPS, Toulouse, France,

10 ⁽⁴⁾ Departamento de Oceanografía Biológica, Centro de Investigación Científica y de Educación
11 Superior de Ensenada, México,

12 ⁽⁵⁾ GEOMAR Helmholtz Centre for Ocean Research, Kiel, Germany.

13

14 Corresponding author: Pierre Damien (pdamien@ucla.edu)

15

16

17 **Key Points :**

- 18 • LCEs trigger a local phytoplankton biomass increase in winter.
- 19 • Chlorophyll variability at surface does not reflect the seasonal cycle of the depth-integrated
20 biomass.
- 21 • Convective mixing and Ekman pumping are key mechanisms to preferentially supply nutrient
22 toward the euphotic layer in LCEs.

23

24

25 **Abstract**

26

27 Surface chlorophyll concentrations inferred from satellite images suggest a strong influence of
28 the mesoscale activity on biogeochemical variability within the oligotrophic regions of the Gulf of
29 Mexico (GoM). More specifically, long-living anticyclonic Loop Current Eddies (LCEs) are shed
30 episodically from the Loop Current and propagate westward. This study addresses the biogeochemical
31 response of the LCEs to seasonal forcing and show their role in driving phytoplankton biomass
32 distribution in the GoM. Using an eddy resolving ($1/12^\circ$) interannual regional simulation, it is shown
33 that the LCEs foster a large biomass increase in winter in the upper ocean. It is based on the coupled
34 physical-biogeochemical model NEMO-PISCES that yields a realistic representation of the surface
35 chlorophyll distribution. The primary production in the LCEs is larger than the average rate in the
36 surrounding open waters of the GoM. This behavior cannot be directly identified from surface
37 chlorophyll distribution alone since LCEs are associated with a negative surface chlorophyll anomaly
38 all year long. This anomalous biomass increase in the LCEs is explained by the mixed-layer response
39 to winter convective mixing that reaches deeper and nutrient-richer waters.

40

41

42

43

44

45

46 **I/ Introduction**

47 Historical satellite ocean color observations of the deep waters of the Gulf of Mexico (roughly
48 delimited by the 200m isobath and from hereafter referred to as GoM open-waters) indicate low surface
49 chlorophyll concentrations ([CHL]), low biomass and low primary productivity (Müller-Karger et al.,
50 1991; Biggs and Ressler, 2001; Salmerón-García et al., 2011). The GoM open-waters are mostly
51 oligotrophic, as confirmed by more recent bio-optical in-situ measurements from autonomous floats
52 (Green et al., 2014; Pasqueron de Fommervault et al., 2017; Damien et al., 2018). The surface
53 chlorophyll concentration in the GoM open-waters exhibits a clear seasonal cycle which is primarily
54 triggered by the seasonal variation of the mixed layer depth (Müller-Karger et al., 2015) and river
55 discharges (Brokaw et al., 2019). In tandem, the seasonal cycle is strongly modulated by the energetic
56 mesoscale dynamic activity which shapes the distribution of biogeochemical properties (Biggs and
57 Ressler, 2001; Pasqueron de Fommervault et al., 2017). This mesoscale activity is dominated by the
58 large and long-living Loop Currents Eddies (LCEs) which are shed episodically by the Loop Current
59 (Weisberg and Liu, 2017) and constitute the most energetic circulation features in the GoM
60 (Sheinbaum et al., 2016; Sturges & Leben, 2000).

61
62 Mesoscale activity (see McGillicuddy et al., 2016 for a review) modulates the phytoplankton
63 biomass distribution (Siegel et al., 1999; Doney et al., 2003; Gaube et al., 2014; Mahadevan, 2014) and
64 the ecosystem functioning (McGillicuddy et al., 1998, Oschlies and Garcon, 1998, Garcon et al., 2001).
65 Specifically, the ability of the mesoscale eddies to enhance vertical fluxes of nutrients is determinant in
66 sustaining the observed phytoplankton growth rate in oligotrophic regions such as the GoM open-
67 waters, where the phytoplankton primary production is limited by nutrient availability in the euphotic
68 layer (McGillicuddy and Robinson 1997; McGillicuddy et al., 1998; Oschlies and Garcon, 1998).

69

70 The upward doming of isopycnals in cyclonic eddies and downward depressions in anticyclonic
71 eddies, also known as “eddy-pumping”, occur when the eddies are strengthening (Siegel et al., 1999,
72 Klein and Lapeyre, 2009) and produce a vertical nutrient transport. This has been historically proposed
73 as the dominant mechanism controlling the mesoscale biogeochemical variability, as it induces a
74 reduction of productivity in the anticyclone and an increase in cyclones. This paradigm is however
75 challenged by observations of enhanced surface chlorophyll concentrations in anticyclonic eddies
76 (Gaube et al., 2014), particularly during winter (Dufois et al., 2016). As a plausible explanation, eddy-
77 wind interactions may significantly modulate vertical fluxes through Ekman transport divergence
78 within the eddies (Martin and Richards, 2001, Gaube et al., 2013, 2015). This mechanism is
79 responsible for a downwelling in the core of cyclones and an upwelling in the core of anticyclones.
80 Dufois et al. (2014, 2016) link these observations to a deeper mixed layer in anticyclonic eddies. This is
81 explained by the eddy-driven modulation of the upper ocean stratification which directly affects the
82 winter convective mixing (He et al., 2017). Observed mixed layers tend to be deeper in anticyclones
83 than in cyclones (Williams, 1998; Kouketsu et al., 2012) and vertical nutrient fluxes to the euphotic
84 layer are potentially enhanced in anticyclones during periods prone to convection (e.g. winter in the
85 GoM). Although some consensus exists on the fundamental role of anticyclonic eddies on the
86 productivity of oligotrophic ocean regions, large uncertainties remain regarding the relative importance
87 of the different mechanisms involved in the biogeochemical responses.

88
89 Besides, in-situ measurements in oligotrophic regions have shown that the surface [CHL]
90 variability, observed from ocean color satellite imagery, is not necessarily representative of the total
91 phytoplankton (carbon) biomass variability in the water column (Siegel et al., 2013; Mignot et al.,
92 2014). In particular, a surface [CHL] winter increase, may result from physiological mechanisms (i.e.
93 modification of the ratio of [CHL] to phytoplankton carbon biomass) or from a vertical redistribution
94 of the phytoplankton (Mayot et al., 2017) rather than from changes in the biomass content. It is not

95 clear yet which of these hypotheses holds in oligotrophic regions, and more specifically in the GoM
96 open-waters where this issue has been addressed by in-situ sub-surface [CHL] observations (Pasqueron
97 de Fommervault et al., 2017). Most of the studies focusing on chlorophyll variability use surface (or
98 near-surface) [CHL] as a proxy for phytoplankton biomass and interpret a [CHL] increase as an
99 effective biomass production. Only a few studies considered the vertically integrated responses (Dufois
100 et al., 2017; Guo et al., 2017; Huang and Xu, 2018) emphasizing the importance of considering the
101 eddy impact on the subsurface.
102

103 The objective of this study is to better understand the role of LCEs in driving [CHL] distribution
104 and variability within the GoM open-waters. Material and methods used in this study are presented in
105 section 2. In section 3, the imprint of the LCEs on the surface [CHL] distribution is inferred from
106 satellite ocean color observations. Since these measurements are confined to the oceanic surface layer
107 and do not allow access to the vertical properties of LCEs, we complete the analysis with a coupled
108 physical-biogeochemical simulation (subsections 2 and 3). Particular attention is paid to the validation
109 of the modeled LCE dynamical structures and surface [CHL] anomalies. In the last section, we propose
110 to disentangle the mesoscale mechanisms controlling the seasonal cycle of the [CHL] vertical profile in
111 LCEs. The model also enables to assess both abiotic and biotic processes and physical-biogeochemical
112 interactions that can be difficult to address with in-situ observations only.
113
114

115 **II/ Material and methods**

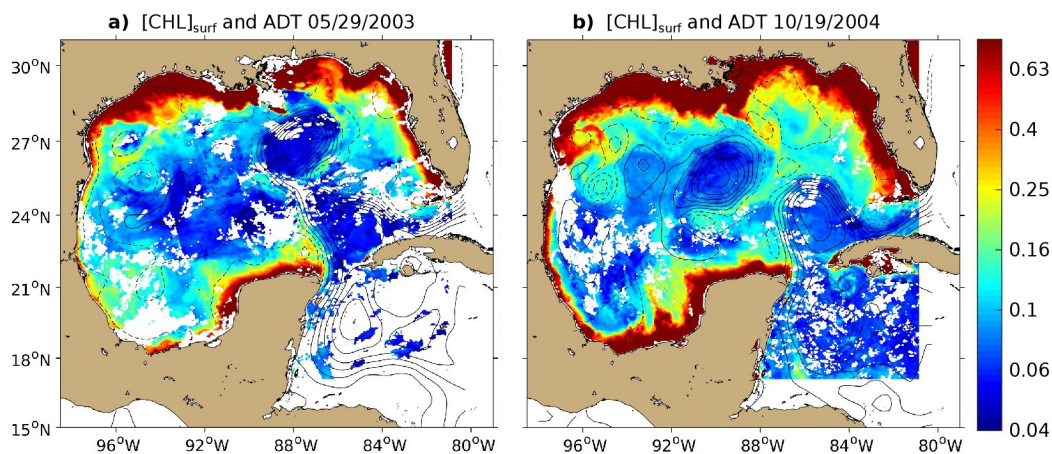
117 **II.1/ The coupled physical-biogeochemical model**

118

119 The simulation analyzed in this study (referred as GOLFO12-PISCES) has been described and
120 compared with observations in Damien et al. (2018). It relies on a physical-biogeochemical coupled
121 model based on the ocean model NEMO (Nucleus for European Modeling of the Ocean, version 3.6;
122 Madec, 2016) and the biogeochemical model PISCES (Pelagic Interaction Scheme for Carbon and
123 Ecosystem Studies; Aumont and Bopp, 2006; Aumont et al., 2015). The model grid covers the GoM
124 and the western part of the Cayman Sea (Fig 1) with a $1/12^\circ$ horizontal resolution (~ 8.4 km). This
125 allows to resolve scales related to the first baroclinic mode, which is of the order of 30-40 km in the
126 GoM open-waters (e.g., Chelton et al., 1998). The model is forced with realistic open-boundary
127 conditions from the MERCATOR reanalysis GLORYS2V3, high frequency atmospheric forcing based
128 on an ECMWF ERA-interim reanalysis (Brodeau et al., 2010), and freshwater and nutrient-rich
129 discharges from rivers (Dai and Trenberth, 2002). The open-boundary conditions of biogeochemical
130 tracers are prescribed from the World Ocean Atlas observation database (Garcia et al., 2010) for NO_3 ,
131 O_2 , Si, and PO_4 , and from the global configuration ORCA2 (Aumont & Bopp, 2006) for DIC, DOC,
132 Alkalinity, and Fe. The other state variables are forced arbitrary very small constant values. The
133 analysis has been performed using 5-day averaged outputs for a period of 5 years from 2002 to 2007.
134 We refer the reader to Damien et al. (2018) for an extended model and numerical setup descriptions. In
135 this previous study, an extensive validation of the modeled properties were carried out , focusing on
136 physical properties that are known to influence primary production and chlorophyll concentration: the
137 mixed layer depth and the depth and slope of the nutricline. A novel aspect was to use in-situ
138 observations collected from autonomous floats and published in Green et al. (2014) and Fommervault
139 et al. (2017) to validate not only the modeled surface chlorophyll concentration but also the chlorophyll
140 vertical profile in the GoM. To be able to reproduce the vertical profile of chlorophyll correctly, the
141 parameters of the biogeochemical model were largely tuned compared to the ones suitable for global
142 simulations (Aumont et al., 2015). The ability of GOLFO12-PISCES to reproduce the main observed
143 features of the GoM was demonstrated, at least at a basin and seasonal scale.

144

145



146 **Figure 1: 8-days composite images of [CHL]_{surf} (in mg·m⁻³) around (a) May 29th 2003 and (b) October 19th 2004 derived from**
147 **Aqua-MODIS images overlaid with contours of Absolute Dynamic Topography (ADT in m) derived from Aviso images are**
148 **superimposed. Contour interval is 10cm and ADT values lower than 40cm are shown with dashed curves.**

149

150 **II.2/ Observational Data Set Used**

151

152 Satellite observations are used to evaluate the ability of GOLFO12-PISCES to reproduce the
153 dynamical and biological signatures associated with LCEs. Surface geostrophic velocities are derived
154 from a 1/4° multi-satellite merged product of absolute dynamic topography (ADT) provided by
155 AVISO+ (<http://marine.copernicus.eu>). Surface chlorophyll concentrations are from the Aqua-MODIS
156 4 km product (Sathyendranath et al., 2012; <http://marine.copernicus.eu>) and consist of 8-day
157 composites from 2003 to 2015.

158

159 **II.3/ LCEs detection, tracking and composite construction**

160

161 In order to track the LCEs, we use the algorithm developed by Nencioli et al. (2010), which has
162 been extensively employed to track coherent mesoscale eddies (Dong et al., 2012, Ciani et al. 2017,
163 Zhao et al. 2018) and submesoscale eddies (Damien et al., 2017). It is based on the geometric
164 organization of the velocity fields, dominated by rotation, that develop around eddy centers. Here, it is
165 applied to weekly AVISO+ surface geostrophic velocities and GOLFO12-PISCES 5-day averaged
166 velocities at 20m depth. The selection of LCEs is defined using the criteria that eddies have to be shed
167 from the Loop Current.

168

169 In order to assess the [CHL] response to LCE dynamics, eddy-centric horizontal images and
170 transects of LCEs are used to make composites constructed by averaging modeled variables of the
171 different LCEs collocated to their center. The transect building procedure involves an axisymmetric
172 averaging that assumes axis-symmetry of the dynamical structures and no tilting of their rotation axis.
173 Moreover, we choose not to consider the LCEs formation period and the LCEs destruction period when
174 reaching the western basin (Lipphardt et al., 2008; Hamilton et al., 2018) as LCE destruction/formation
175 involves specific processes (Frolov et al., 2004; Donohue et al., 2016). We therefore focus on the LCEs
176 contained in the central part of the GoM from 86°W to 94°W. Annual composites are computed along
177 with monthly composite averages in order to assess seasonal variability. Composite LCEs averaged
178 during the months of January and February are referred to as winter composites and those averaged
179 during July and August are referred to as summer composites. These composites provide an overview
180 of the LCEs mean hydrographical, biogeochemical and dynamical characteristics.

181

182 **II.4/ Diagnostics**

183

184 The LCE radius R_{LCE} is estimated as the radial distance between the center and the peak
 185 azimuthal velocity V_{max} . The mixed layer depth (MLD), a major physical factor influencing nutrient
 186 distribution and [CHL] dynamics (Mann and Lazier, 2006), is defined as the depth at which potential
 187 density exceeds its value at 10m depth by $0.125 \text{ kg}\cdot\text{m}^{-3}$ (Levitus, 1982; Monterey and Levitus, 1997).
 188 The stratification of the water column is evaluated by the square of the buoyancy frequency

189 $N^2(z) = \frac{-g}{\rho_0} \frac{\partial \rho}{\partial z}$, where g is the gravitational acceleration, z is depth, ρ is density and ρ_0 is a reference
 190 density.

191

192 As carried out in Damien et al. (2018), several metrics are defined and used to describe [CHL]:

- 193 • [CHL]_{surf}: [CHL] averaged between 0 and 30 m depth, and considered as surface concentration
 194 (in $\text{mg CHL}\cdot\text{m}^{-3}$),
- 195 • [CHL]_{tot}: integrated content of [CHL] over the 0-350 m layer (in $\text{mg CHL}\cdot\text{m}^{-2}$),
- 196 • DCM: depth of the Deep Chlorophyll maximum (in m),
- 197 • [CHL]_{DCM}: [CHL] value at DCM depth (in $\text{mg CHL}\cdot\text{m}^{-3}$).

198 To understand the mesoscale distribution of [CHL], key biological variables are vertically integrated
 199 between 0 and 350m: the phytoplanktonic concentration [PHY]_{tot}, the primary production rate PP_{tot} and
 200 the grazing rate GRZ_{tot} . PP_{tot} consists of two components: new production PPN_{tot} fueled by nutrients
 201 supplied from a source external to the mixed layer and regenerated production PPR_{tot} sustained by
 202 recycled nutrients within the euphotic layer (Dugdale & Goering, 1967; Eppley & Peterson, 1979). The
 203 euphotic depth corresponds to 1% of the incoming photosynthetic active radiation at surface and
 204 reaches between 120 and 150 m in the GoM (Jolliff et al., 2008; Linacre et al., 2019). A chlorophyll
 205 concentration anomaly within LCEs, [CHL]', is computed as $[CHL]' = [CHL] - \overline{[CHL]}$, where $\overline{[CHL]}$ is
 206 the averaged background [CHL] field in the open GoM waters (for radius > 250km from the LCEs'

207 centers). We also define the normalized anomaly as $[CHL]' / SD([CHL]')$ with SD the standard deviation
208 operator, following a similar approach as Gaube et al. (2013, 2014) and Dufois et al. (2016). To limit
209 the influence of very high [CHL] values in coastal waters under the direct influence of continental
210 discharges, a salinity filtering criterion (lower than 36 psu) is applied. A similar method was used by
211 Gaube et al. (2013, 2014) to filter edge effects but using a distance criterion instead.

212

213 **III/ Results**

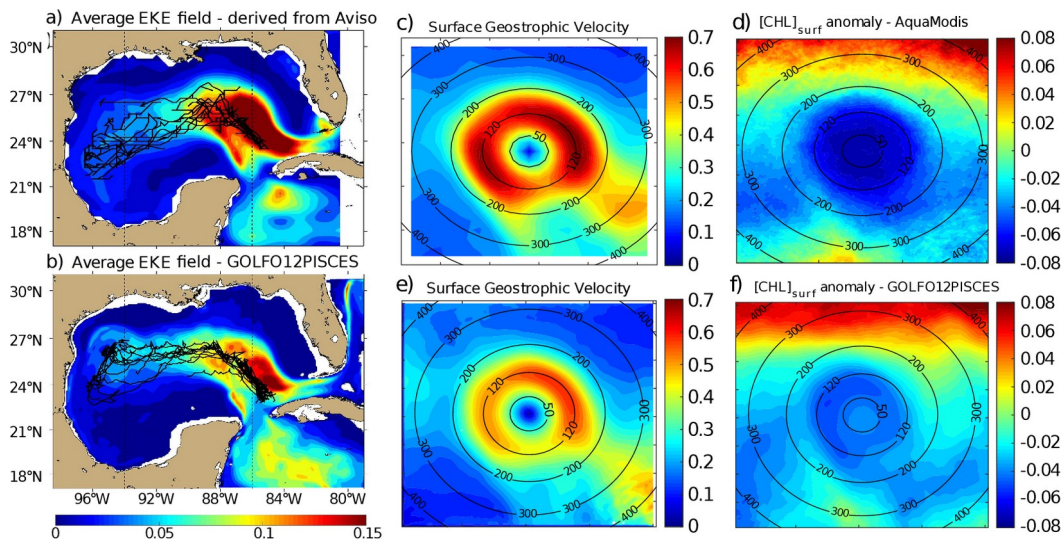
214

215 **III.1/ Satellite observations of [CHL]**

216

217 Fig 1 shows the 8-day averaged satellite observations of the surface chlorophyll around May 29th
218 2003 (a) and October 19th 2004 (b). These observations highlight the strong contrast between the
219 eutrophic conditions in the coastal waters and the oligotrophic conditions in the open ocean, as already
220 addressed by several studies (Martinez-Lopez & Zavala-Hidalgo, 2009; Pasqueron de Fommervault et
221 al., 2017). Far from the coast, these figures also reveal that the surface chlorophyll varies at a scale of
222 the order of 100km with a distribution that tends to follow the absolute dynamic topography (ADT)
223 contours.

224

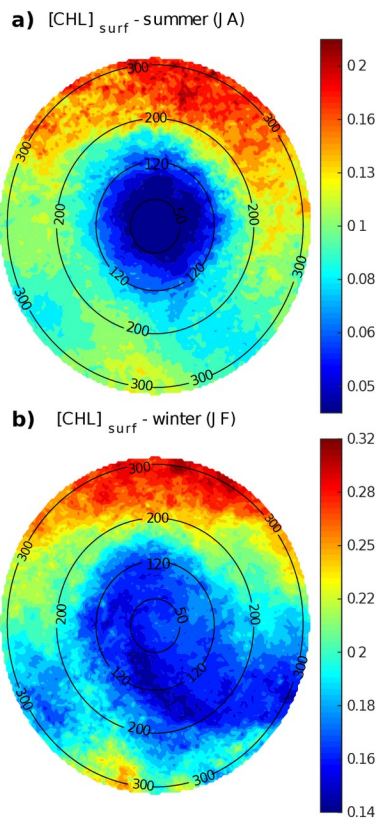


225 **Figure 2: Average eddy kinetic energy (EKE) field derived from (a) Aviso geostrophic surface velocities and from (b) GOLFO12-**
 226 **PISCES currents at 10m depth. The trajectories of the tracked LCEs are superimposed to the EKE field (black lines). Vertical**
 227 **black dashed lines indicate the central GoM area over which composites are built. Annual LCE composite images of surface**
 228 **geostrophic velocities for (c) Aviso images and (e) GOLFO12-PISCES. Annual LCE composite images of surface chlorophyll**
 229 **concentration anomaly for (d) Modis images and (f) GOLFO12-PISCES. Black circles indicate the radius in kilometers.**

230

231 LCEs trajectories are reported on Fig 2.a, superimposed onto the geostrophic climatological eddy
 232 kinetic energy (EKE) field at the surface. EKE is computed from eddy velocities defined on each grid
 233 cell as the difference between the total horizontal current and its mean value over 120 days. This time
 234 window is chosen to filter the seasonal signal. EKE is concentrated in the LC and on the westward
 235 pathway of the LCEs (Lipphardt et al. 2008) demonstrating that LCEs constitute the major source of
 236 EKE in the GoM open waters (Sheinbaum et al., 2016; Sturges & Leben, 2000; Hamilton, 2007;
 237 Jouanno et al., 2016).

238



239 **Figure 3: LCE composite images of $[CHL]_{surf}$ derived from Aqua-MODIS for the (a) summer and (b) winter seasons. Black circles**
 240 **indicate the radius in kilometers.**

241

242 LCE annual composites of surface geostrophic velocities (Fig 2.c) and $[CHL]_{surf}$ (Fig 2.d) are
 243 built from 482 different satellite images. On average, we found that $R_{LCE} \sim 120$ km and $V_{max} \sim 0.6-0.7$
 244 $m \cdot s^{-1}$, in agreement with previously reported LCEs (Elliot, 1982; Cooper et al., 1990; Forristal et al.,
 245 1992; Glenn and Ebbesmeyer, 1993; Weisberg and Liu, 2017; Tenreiro et al., 2018). LCEs are
 246 associated with a negative $[CHL]_{surf}$ anomaly (~ -0.07 $mg \cdot m^{-3}$ in the annual average). The LCEs
 247 influence on $[CHL]_{surf}$ is largest in summer (Fig 3.a) when it reaches very low values (< 0.045 $mg \cdot m^{-3}$),
 248 which corresponds to an anomaly of ~ -0.08 $mg \cdot m^{-3}$. This anomaly is less remarkable in winter (~ -0.06
 249 $mg \cdot m^{-3}$, Fig 3.b) when $[CHL]_{surf} \sim 0.17$ $mg \cdot m^{-3}$ within LCEs. The high chlorophyll concentrations in the
 250 northern part of the composites (in the southern part too but in smaller proportions) are related to
 251 shelves.

252

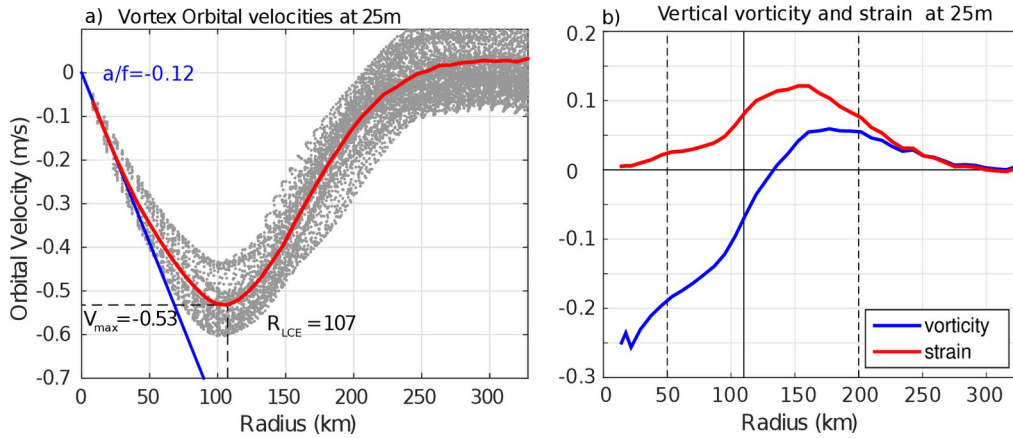
III.2/ Dynamical characterization of modeled LCEs

A total of 11 model LCEs were detected during the 5 years of simulation. Their trajectories are reported in Fig 2.b, superimposed upon the climatological EKE field simulated at 10 meters. The westward / southwestward propagation of LCEs is well reproduced (Vukovich, 2007) even though the LCEs translation is almost westward in GOLFO12-PISCES. Comparison with Fig 2.a shows the ability of GOLFO12-PISCES to represent the mean and transient dynamical features of the GoM open waters (also see Garcia-Jove et al., 2016).

The robustness of the composite method arises from the number of LCE used to build the composites:

- Annual composite is built from 605 5-day averaged LCEs model outputs from 10 different LCEs,
- Summer composite is built from 83 5-day averaged LCEs model outputs from 8 different LCEs,
- Winter composite is built from 93 5-day averaged LCEs model outputs from 9 different LCEs.

The model LCEs surface geostrophic velocities (Fig 2.e) have important similarities with velocities inferred from altimetry (Fig 2.c) confirming that GOLFO12-PISCES reproduces the surface signature of the LCEs. However, one can also notice an underestimation of the surface orbital velocities ($\sim 25\%$ on average over the 50-200 km radius range). This bias could result from the relatively coarse model resolution and 5-day output frequency that are unable to fully capture the gradient intensity at R_{LCE} . The assumption of an axial symmetry of the LCE circulation around its center also induces an error that tends to decrease V_{max} .



278 **Figure 4: (a) Orbital velocities at 25m depth in function of the radius of each detected LCE (light gray dots). The red line is the**
 279 **LCE orbital velocity profile of the annually-averaged composite. (b) Vertical vorticity and strain computed from the averaged**

280 **orbital velocity profile assuming no radial velocity in cylindrical coordinates as $\zeta_z = \frac{1}{f r} \frac{\partial r v}{\partial r}$ and $S = \frac{1}{f} \left(\frac{\partial v}{\partial r} - \frac{v}{r} \right)$.**

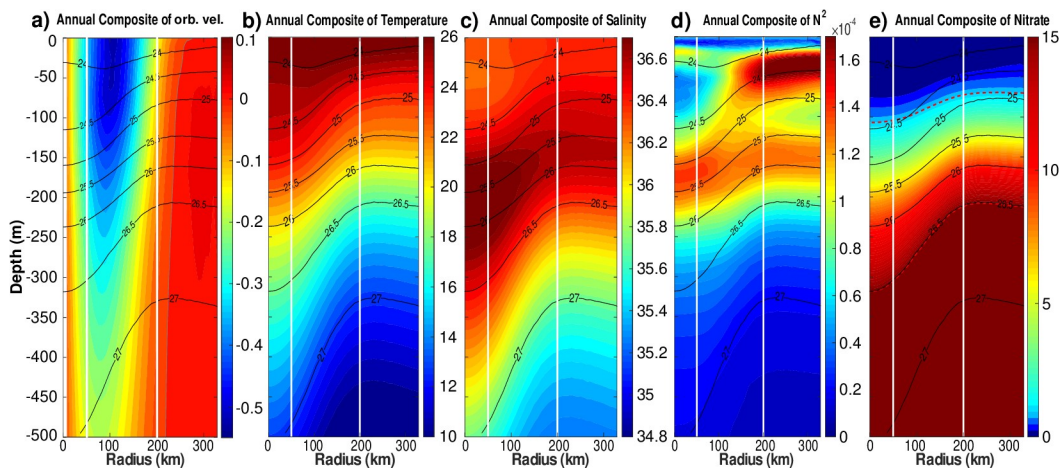
281

282 Orbital velocities of composite eddies are used to distinguish different dynamical areas within
 283 LCEs. The model annual average dynamical profile at 25m depth (Fig 4) reveals a typical vortex-like
 284 structure with $R_{LCE} \sim 107$ km and $V_{max} \sim 0.53$ m·s⁻¹ and suggests the following decomposition:

- 285 • $r < 50$ km : the **LCEs core**, where the eddy is approximately in solid body rotation: $V_{orb} = a \cdot r$
 286 where the coefficient a is related to the Rossby number ($Ro = 2a/f$). The ratio a/f is estimated
 287 to be ~ -0.12 (Fig. 4). In this field, the strain is reduced to a minimum and the flow is dominated
 288 by rotation.
- 289 • 50 km $< r < 200$ km: the **LCEs ring** structure where the orbital velocity reaches its maximum
 290 at R_{LCE} and then decreases. The horizontal strain is important in this field, even dominating
 291 vorticity from radius exceeding R_{LCE} .
- 292 • $r > 200$ km: the **background GoM**, where the velocity anomalies related to the LCE vanish.

293

294 In the vertical (Fig 5.a), LCEs are near-surface intensified anticyclonic vortex rings. At depth,
 295 the orbital peak velocity decreases rapidly. At 500 m depth, $V_{\max} \sim 0.17 \text{ m}\cdot\text{s}^{-1}$ and $R_{\text{LCE}} \sim 75 \text{ km}$, and
 296 the dynamical LCE signal nearly vanishes below 1500 m depth ($V_{\max} < 0.03 \text{ m}\cdot\text{s}^{-1}$). The proposed
 297 division into 3 distinct dynamical regions applies from the surface down to 500 m depth (Fig 5.a).



298 **Figure 5: Annually-averaged LCE composite transects of (a) orbital velocities [m/s], (b) potential temperature [°C], (c) salinity**
 299 **[psu], (d) squared Brunt-Väisälä frequency (N^2 in s^{-2}) and (e) nitrate concentration [$\text{mmol}\cdot\text{m}^{-3}$]. Isopycnals anomalies (black**
 300 **contours) are superimposed on all panels. Vertical white lines delimit the three dynamical fields of the LCE composite. On panel**
 301 **e, dashed red lines highlights two specific iso-nitrate contours: 1 and $15 \text{ mmol}\cdot\text{m}^{-3}$.**

303 The composite hydrological structure of modeled LCEs is shown in Fig 5.b and 5.c. The
 304 depression of isopycnals, associated with a depression of isotherms and isohalines, is characteristic of
 305 oceanic anticyclones. In the core of the eddies, the composite depicts a salinity maximum located
 306 between 100 and 300 m, corresponding to the signature of the Atlantic Subtropical UnderWater
 307 (ASTUW) of Caribbean origin entering the GoM through the Yucatan Channel (Badan et al., 2005;
 308 Hernandez-Guerra & Joyce, 2000; Wuust, 1964). This salinity maximum is not limited to the core of
 309 the LCE but gradually erodes and shallows: 36.82 psu at 200 m in the LCEs core and 36.61 psu at 150
 310 m in the background GoM common water. Details on the fate of this salinity maximum investigated
 311 with GOLFO12 simulations can be found in Sosa-Gutiérrez et al. (2020). The ASTUW layer (salinity >

312 36.5 psu) is also thicker in the LCEs core (~190 m thick) compared to the background GoM water
313 (~120 m thick). Overall, GOLFO12-PISCES reproduces the observed hydrological structure of LCEs
314 (Elliott, 1982; LeHenaff et al., 2012; Hamilton et al., 2018; Meunier et al., 2018b).

315

316 The annually averaged LCE composite presents a lens-shaped structure exhibiting a ~50 m thick
317 layer of weakly stratified waters located between 50 and 100 m depth (Fig 5.d). This subsurface modal
318 water presents hydrological characteristics close to the observed background GoM waters (potential
319 temperature ~25.4°C and salinity ~ 36.3 psu, Meunier et al., 2018b) and is surrounded below and above
320 by well stratified layers (Meunier et al., 2018a). The upper pycnocline varies seasonally and vanishes in
321 winter due to the deepening of the mixed layer, whereas the lower pycnocline is permanent.

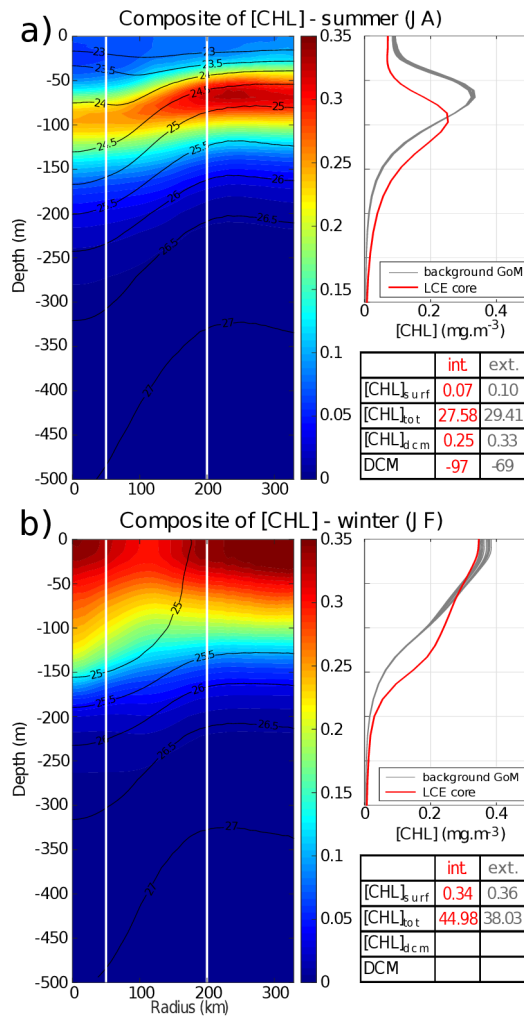
322

323 The downward displacement of isopycnals is accompanied by a depletion of nutrients in the
324 upper layer of the LCEs core (Fig 5.e). This is a typical feature of mesoscale anticyclones in the ocean
325 (McGillicuddy et al. 1998; Oschlies and Garcon, 1998). The 1 mmol.m⁻³ iso-nitrate concentration
326 (hereafter Z_{NO_3} , sometimes referred to as the nitracline as in Cullen & Eppley, 1981; Pasqueron de
327 Fommervault et al., 2017 or Damien et al., 2018) is located at ~ 70 m depth in the background GoM
328 waters whereas it is found much deeper in the core ($Z_{NO_3} \sim 106$ m). At depth, iso-nitrate layers and
329 isopycnals are well correlated (Ascani et al., 2013; Omand & Mahadevan, 2014). For instance, iso-
330 nitrate concentration of 15 mmol·m⁻³ follows the displacements of the 1026.5 kg·m⁻³ isopycnal.
331 However, above 150 m, the density/nitrate relation is different inside and outside the eddies (Z_{NO_3} is
332 collocated with isopycnal 1024.4 kg·m⁻³ in the LCEs core while it is on isopycnal 1024.9 kg·m⁻³ in the
333 background GoM).

334

335 **III.3/ Surface and vertical distribution of chlorophyll in LCEs**

336



337 **Figure 6: LCE composite transects of [CHL] during summer season (A) and winter season (B). Density anomalies (black**
 338 **contours) are superimposed. Vertical white lines delimit the three dynamical fields of the LCE composite. For each season, [CHL]**
 339 **profiles in the LCE core ($r < 50$ km, red lines) and in the background GoM ($200 \text{ km} < r < 330$ km, gray lines) are plotted. Key**
 340 **metrics concerning [CHL] profiles are also indicated in the tables.**

341

342 The large difference in stratification between the LCEs core and background GoM suggests a
 343 contrasted seasonal response of the [CHL]. This is evidenced by the analysis of summer and winter
 344 composites of [CHL] vertical distribution:

- 345 • In summer (Fig 6.a), $[CHL]_{surf}$ is $\sim 30\%$ lower in the LCEs core ($r < 50\text{km}$) than in the
 346 background GoM ($200 \text{ km} < r < 330$ km). A pronounced DCM, characteristic of oligotrophic
 347 environments, is deeper in the core (~ 97 m) than in the background GoM (~ 69 m) with
 348 chlorophyll concentrations significantly lower in the interior ($\sim - 25\%$).

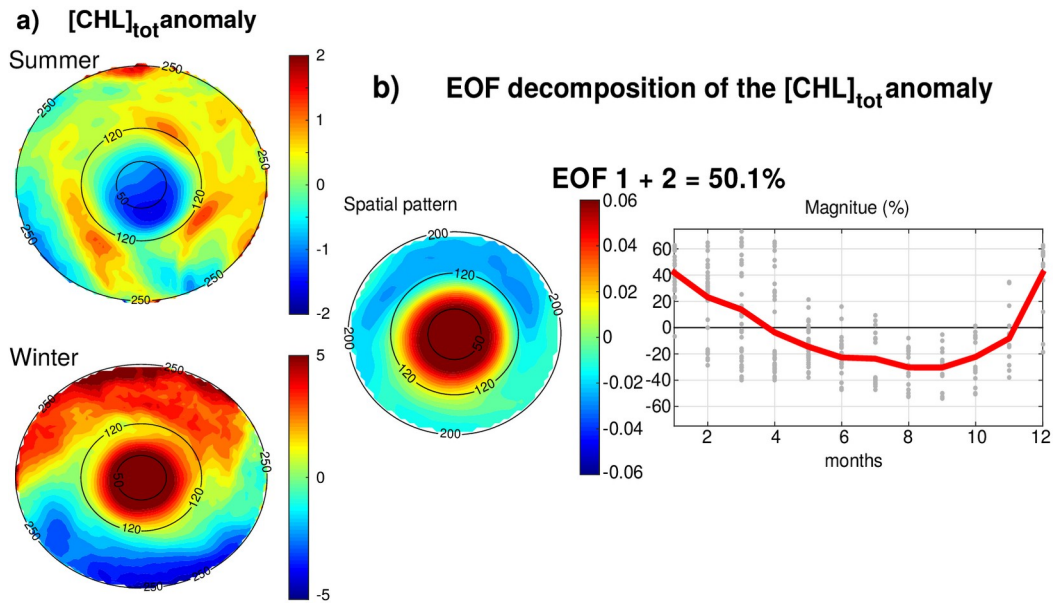
349 • In winter, the [CHL] is maximum at the surface in all the composite domains (Fig 6.b).
350 [CHL]_{surf} is lower in the LCEs core compared to the background GoM but the difference is less
351 marked (~ - 6%) than in summer. The main discrepancy is the depth of the inflection point of
352 these profiles. It is deeper in the LCEs core (~-150 m), resulting in a more homogenized [CHL]
353 over a deeper layer than in the background GoM (~-120 m).

354

355 However, despite reduced surface concentration both in winter and summer, the integrated
356 chlorophyll content, [CHL]_{tot}, shows a distinct seasonal pattern compared to the surface (tables in Fig
357 6):

- 358 • In summer, [CHL]_{tot} is lower in the LCEs core (27.58 mg·m⁻²) compared to the background
359 GoM (29.41 mg·m⁻²) and $\Delta[\text{CHL}]_{\text{tot}} = -1.83 \text{ mg}\cdot\text{m}^{-2}$,
- 360 • In winter, [CHL]_{tot} is higher in the LCEs core (44.98 mg·m⁻²) compared to the background GoM
361 (38.03 mg·m⁻²) and $\Delta[\text{CHL}]_{\text{tot}} = + 6.95 \text{ mg}\cdot\text{m}^{-2}$.

362 The winter increase of [CHL]_{tot} is around 29% in the background GoM whereas it reaches 63% in the
363 LCEs core, leading to [CHL]_{tot} in the core being larger than [CHL]_{tot} in the background GoM in winter.
364 Meanwhile, [CHL]_{surf} remains lower within the LCEs core. The fact that the [CHL] at the surface does
365 not reflect its depth-integrated behavior means that the peculiar variability of [CHL] within LCEs may
366 not be fully captured by ocean color satellite measurements. This is consistent with Pasqueron de
367 Fommervault et al. (2017) and Damien et al. (2018) observations and modeling results which addressed
368 the vertical [CHL] distribution in the GoM.

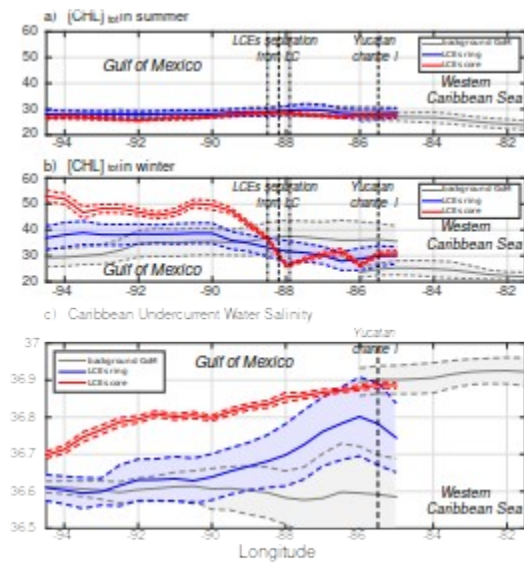


370 **Figure 7: (a) Anomaly of $[\text{CHL}]_{\text{tot}}$ in summer and winter seasons. Black circles indicate the radius in kilometers. (b) EOF**
 371 **decomposition of the normalized $[\text{CHL}]_{\text{tot}}$ anomaly. The spatial patterns and monthly magnitude (gray dots; the red line**
 372 **represents their monthly averaged value) of the two first modes are indicated. Modes 1 and 2 were summed together (upper**
 373 **panel) and represent 50.1% of the total variance.**

374

375 $[\text{CHL}]_{\text{tot}}$ is strongly shaped by both the seasonal variability and the LCEs. The seasonal
 376 composites of $[\text{CHL}]_{\text{tot}}$, shown in Fig 7.a, confirm the summer/winter contrast and highlight a
 377 monopole structure with a relatively homogeneous distribution of $[\text{CHL}]_{\text{tot}}$ within the eddy's core. In
 378 order to better characterize the spatio-temporal variability of $[\text{CHL}]_{\text{tot}}$ induced by LCEs, an Empirical
 379 Orthogonal Function (EOF) analysis was performed on the normalized $[\text{CHL}]_{\text{tot}}$ anomaly (Fig 7.b)
 380 following the methodology of Dufois et al. (2016). It consists in decomposing the signal into
 381 orthogonal modes of variability. Here, we choose to focus on the first two most significant modes
 382 which explain 40.2% and 9.9% of the variability. Since they both depict a similar monopole structure
 383 in the LCEs core, they were added up in a mode referred to EOF 1+2 responsible for 50% of the total
 384 $[\text{CHL}]_{\text{tot}}$ variance within LCEs. The third eigenmode (not shown) accounts for 6.2% and depicts a
 385 dipole structure with opposite polarity located at the east and north of the eddy center. On average, the

386 EOF1+2 mode is positive in winter (from December to March) and negative the rest of the year (from
 387 April to November), with a maximum in January December and a minimum in September. This
 388 justifies, a posteriori, the choice to consider winter and summer LCE composites.
 389



390 **Figure 8: (a) Summer $[CHL]_{tot}$, (b) winter $[CHL]_{tot}$ and (c) salinity of Caribbean waters (ASTUW defined as the subsurface**
 391 **salinity maximum) as a function of longitude in (red) the LCEs core, (blue) the LCEs ring and in (gray) the background GoM.**
 392 **Full lines indicate the averaged value and dashed lines the +/- one standard deviation interval.**

393
 394

395 The composite evolution of the LCEs $[CHL]_{tot}$ along their westward journey is shown in Fig 8.a
 396 and 8.b. It illustrates how the total chlorophyll concentration is preferentially increased in winter within
 397 the LCEs core, as soon as the LCEs are shed from the LC. The winter $[CHL]_{tot}$ within LCEs is much
 398 larger (exceeding one standard deviation) than the background winter $[CHL]_{tot}$. In terms of integrated
 399 $[CHL]$, the LCEs-induced seasonal variability overwhelms the GoM open-waters background seasonal
 400 variability.

401

402 **IV/ Discussion**

403

404 In an oligotrophic environment such as the GoM open-waters, the primary production is
405 generally limited by nutrient supply and $[\text{CHL}]_{\text{tot}}$ exhibits low seasonal variability at the GoM basin
406 scale (Pasqueron de Fommervault et al., 2017). The winter increase of $[\text{CHL}]_{\text{tot}}$ within the LCEs core
407 (which translates into an effective increase of biomass, see appendix A) contrasts and may have large
408 implications for the regional biogeochemical cycles and ecosystem structuration. It also echoes several
409 studies which report elevated $[\text{CHL}]_{\text{surf}}$ within anticyclonic eddies in the oligotrophic subtropical gyre
410 of the southeastern Indian Ocean (Martin and Richards, 2001; Waite et al., 2007; Gaube et al., 2013;
411 Dufois et al., 2016, 2017; He et al., 2017), questioning the classical paradigm of low productivity
412 usually associated with anticyclonic eddies.

413

414 The mechanisms explaining the LCE impact on $[\text{CHL}]$ are discussed below, trying to rationalize
415 the respective role of abiotic (e.g., trapping, winter mixing, Ekman pumping) and biotic processes (e.g.,
416 primary production (PP), grazing pressure, regenerated versus new PP).

417

418

419 **IV.1 Eddy trapping**

420

421 The distinct hydrological and biogeochemical properties associated with the LCEs core suggest
422 their ability to trap and transport oceanic properties. This mechanism, known as the eddy-trapping
423 (Early et al., 2011; Lehahn et al., 2011; McGillicuddy, 2015; Gaube et al., 2017), is efficient only if the
424 orbital velocities of the vortex are faster than the eddy propagation speed (Flierl, 1981; d'Ovidio et al.,
425 2013). The rotational velocities of the model LCEs are $\sim 0.53\text{m}\cdot\text{s}^{-1}$ are one order of magnitude larger
426 than the propagation velocities ($\sim 0.046\text{m}\cdot\text{s}^{-1}$ on average). This suggests that LCEs might have a

427 certain ability to trap the water masses present in their core with relatively low exchanges with the
428 exterior.

429

430 Salinity is well-suited to investigate water masses trapped within the LCEs core during their
431 propagation toward the western GoM (Fig 8.c; Sosa-Gutierrez et al., 2020): salinity distribution shows a
432 marked subsurface maximum that is not affected by biogeochemical processes. In the Western
433 Caribbean Sea, ASTUW is characterized by high salinity (~ 36.9 psu on average) and low standard
434 deviation (< 0.05 psu). The eastern GoM salinity field reveals that most of the ASTUW crosses the
435 Yucatan Channel within the Loop Current. During the formation of LCEs, a significant part of
436 ASTUW is captured into the LCEs core with low alteration of its properties (Fig 5.c and 8.c). Within
437 the LCEs core, the water mass is transported from eastern to the western GoM where its salinity
438 decreases from 36.9 psu to 36.7 psu. Although altered, the ASTUW signature is still clearly detectable
439 in the GoM western boundary. The other part of ASTUW entering the GoM is found in the LCEs ring.
440 Compared to the core, the salinity in the ring is on average lower (~ 36.8 psu in the eastern GoM) and
441 presents a high standard deviation, pointing out that more recent ASTUW co-exists with older ASTUW
442 that yields lower salinity maxima. As LCEs travel westward across the GoM, salinity in the LCEs ring
443 decays rapidly to reach values similar to the background GoM values (~ 36.6 psu). This
444 homogenization mainly arises from vertical mixing and winter mixed layer convection (Sosa-Gutierrez
445 et al., 2020). Horizontal intrusions and filamentation may also contribute to this homogenization
446 (Meunier et al., 2020). The composites also suggest that almost no ASTUW enters the GoM apart from
447 the LCEs. The slight increase of the background salinity from eastern to western GoM is a consequence
448 of the diffusion of salt from the LCEs toward the exterior.

449

450 Although LCEs undergo considerable decaying rates, their erosion is particularly strong in the
451 ring while the core remains better isolated from the surrounding waters (Lehahn et al., 2011; Bracco et

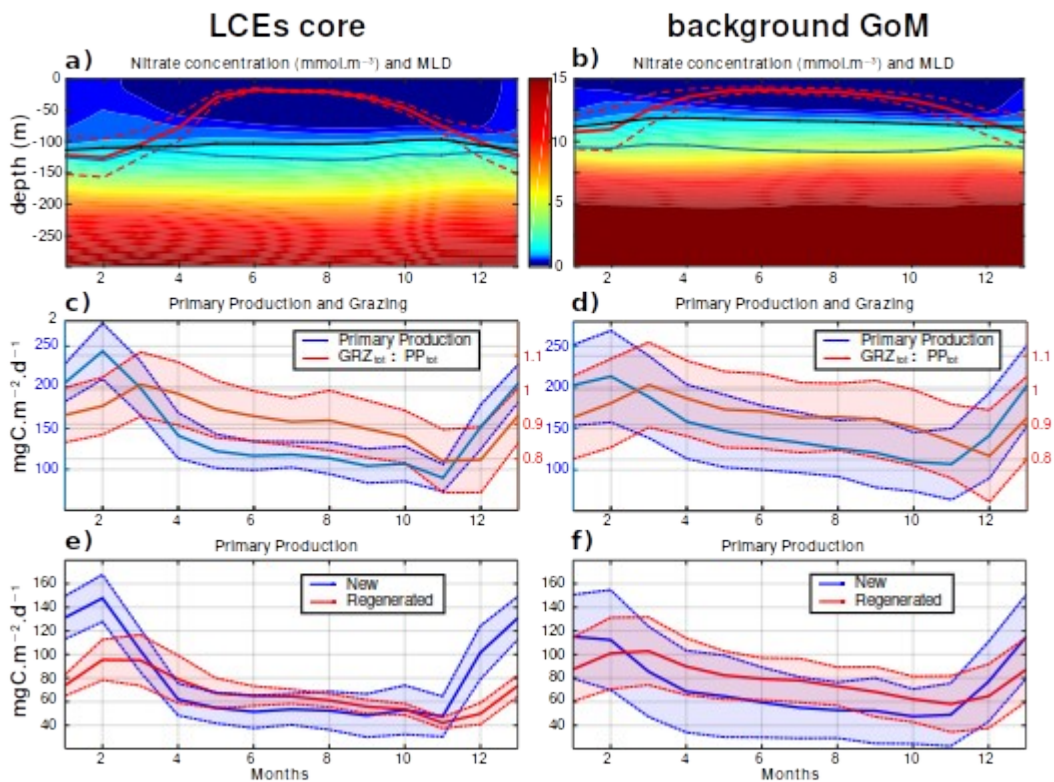
452 al., 2017). Since no significant $[CHL]_{tot}$ seasonal variability is reported in the Western Caribbean Sea
 453 (Fig. 8), the biogeochemical behavior in the LCEs core has then to be driven by local processes with
 454 low influence of horizontal advective process from the ring or of the Caribbean waters trapped during
 455 the LCEs formation. Given that the LCEs core is also quite homogeneous, the following discussion
 456 relies on the analysis of the seasonal cycles of selected parameters averaged within the LCEs core.

457

458

459

IV.2 Nitracline depth and nutrient supply into the mixed layer



461 **Figure 9:** Climatological seasonal cycles of (a and b) nitrate concentration profiles (the red line overlaid is the average mixed layer
 462 depth, the blue line is the base of the euphotic layer and the black line the nitracline), (c and d) the total primary production
 463 (blue) and the ratio of grazing rate over primary production (red) and (e and f) the new (blue) and regenerated (red) primary
 464 production. The left panels (a, c and e) refer to the seasonal time series in the LCEs core ($r < 50$ km) whereas the right panels (b, d

465 and f) refer to the seasonal time series in the background GoM ($r > 200$ km). For each average cycle, the mean value is shown (full
466 line) along with its variability (± 1 standard deviation relative to the mean, dashed lines).

467

468 The LCEs impact the upper ocean stratification (Fig 5.d), the nutricline depth (Fig 5.e) and
469 consequently the nutrient supply to the euphotic layer (McGillicuddy et al., 2015). The relationship
470 between mixed layer deepening and nutrient supply is studied here by comparing the Z_{NO_3} with the
471 MLD (Fig 9.a,b).

472

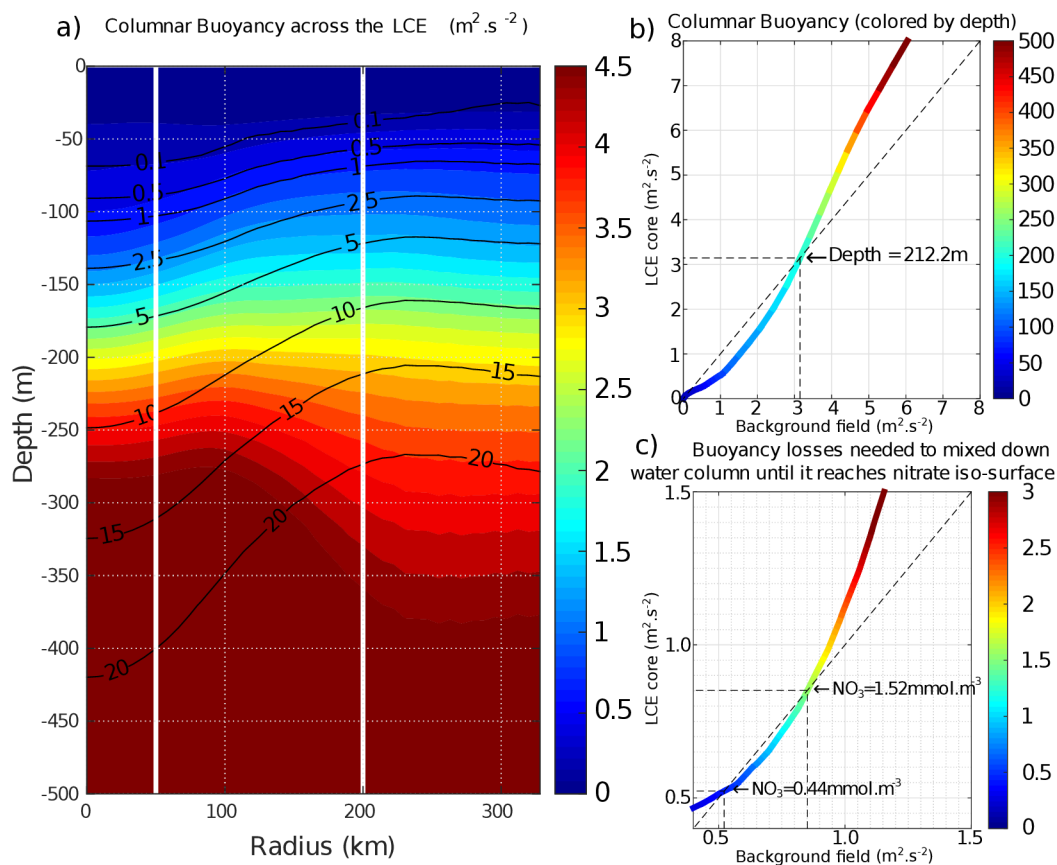
473 In late-spring and summer (from May to September), the water column is stratified (shallow
474 MLD) and the downward displacement of the isopycnals within the LCEs pushes nutrients below the
475 euphotic zone (see also Figs 5.e, 6.a): less nutrients are available within the LCE cores for
476 phytoplankton growth, explaining a deeper and less intense DCM. In winter, the convective mixing,
477 fostered both by intense buoyancy losses and strong mechanical energy input at the surface, causes a
478 larger deepening of the mixed layer within the LCEs core (~ -125 m, Fig 9.a) compared to the
479 background (~ -85 m, Fig 9.b). This asymmetry is due to a pronounced decrease of the surface and
480 subsurface stratification within the LCE core (Fig 5.d, Kouketsu et al., 2012). A quantitative diagnostic

481 of the stratification is given by the columnar buoyancy, $\int_0^H N^2(z) \cdot z \cdot dz$ which measures the buoyancy

482 loss required to mix the water column to a depth H (Herrmann et al. 2008). Fig 10.a reveals significant
483 differences in pre-winter buoyancy between the eddy core and its surroundings. Assuming that the
484 change in buoyancy content is mainly controlled by the buoyancy flux at the surface (see Turner 1973;
485 Lascaratos & Nittis, 1998), it suggests that mixing the water column down to ~ -210 m depth requires
486 smaller surface buoyancy loss in LCEs cores compared to the background GoM (Fig 10.b).

487

488 However, the larger winter deepening of the mixed layer within the LCEs core is not a sufficient
 489 condition to explain a larger nutrient supply. Indeed, it fosters the transport of nutrients from the
 490 nitracline toward the mixed layer because both are getting closer. Fig 10.c highlights that a smaller
 491 buoyancy loss mixes down the water column to greater nutrient concentration levels in the LCEs core
 492 compared to the LCEs surrounding. This likely explains the winter increase of surface nitrate
 493 concentration within the LCEs (Fig 9.a). In addition, a diagnostic of the different contributions to
 494 $[\text{NO}_3]$ evolution is proposed in appendix B. It shows the dominant role of vertical advection and
 495 diffusion in winter in providing nutrients to the euphotic layer in the LCEs core.



497 **Figure 10: (a) Columnar Buoyancy transect composite in summer, corresponding to pre-winter mixing season. Iso-nitrate**
 498 **concentrations (black contours) are superimposed. Vertical white lines delimit the three dynamical fields of the LCE composite.**
 499 **(b) Vertical increase of the columnar buoyancy in the LCEs core versus the background GoM. Colors refer to depth. (c)**
 500 **Columnar buoyancy loss required to mix the water column down to the iso-nitrate surface defined by the line color.**

501
502
503
504
505
506
507
508
509
510
511
512
513
514
515
516
517
518
519
520
521
522
523

So far we have assumed that the surface buoyancy fluxes are identical over the LCEs core and the background GoM. However, this is not strictly the case because temperature/salinity features in the LCEs and background waters are different (Fig 5.b,c; see also Williams 1988). The modeled surface buoyancy loss during winter season is ~18 % more intense within the LCEs. This difference is substantial and probably mainly driven by additional surface cooling applied on the warm LCE core through air-sea interaction. It contributes to enhance convection within the eddies core, and then nutrient supply toward the surface.

IV.3 Productivity and grazing

The primary productivity PP_{tot} presents a clear seasonal cycle both in the LCEs cores and in the background GoM with lower values in October-November, a sharp increase starting in November, a maximum in February and a gradual decrease from March to October (Fig 9.c.d). The annual PP_{tot} is slightly lower in the LCEs core ($\sim 142.4 \text{ mgC}\cdot\text{m}^{-2}\cdot\text{d}^{-1}$) than in the background GoM ($\sim 148.9 \text{ mgC}\cdot\text{m}^{-2}\cdot\text{d}^{-1}$). The amplitude of the seasonal cycle is larger in the LCEs core: from April to November, PP_{tot} is on average ~12% lower in the LCEs core whereas, in winter, PP_{tot} is ~14% higher where it reaches $\sim 243.2 \text{ mgC}\cdot\text{m}^{-2}\cdot\text{d}^{-1}$ in February. Particularly in the LCE core, the PP_{tot} seasonal cycle is tightly correlated with vertical mixing revealing the important role of mixing in the biogeochemistry. The relatively low standard deviation of the monthly PP_{tot} distribution in the LCE core also supports the idea that the influence of the seasonal variability of the forcing largely overwhelms their interannual and sub-monthly variability (Fig 9.c).

524 The ratio of the PPN_{tot} and PPR_{tot} provides information about the mechanisms controlling the
525 biomass growth (Fig 9.e and 9.f). In winter, the PPN_{tot} plays a leading role, reaching up to 113-147
526 $mgC \cdot m^{-2} \cdot d^{-1}$, driven by the winter mixing and induced NO_3 fluxes (see Appendix B). Conversely, the
527 PPR_{tot} is dominant from April to October. During this period, low NO_3 resources are available in the
528 euphotic layer and the ecosystem preferentially uses ammonium to sustain the PP_{tot} . This seasonal
529 pattern is characteristic of oligotrophic environments such as the GoM open waters (Wawrik et al.,
530 2004; Linacre et al., 2015). In winter, changes in PP_{tot} are correlated to the intensity of winter mixing in
531 the LCEs core (Fig 9.c) and the background GoM (Fig 9.d). The larger PPN_{tot} in the eddy core is
532 consistent with a larger supply of NO_3 and evidences that the core of anticyclones can be preferential
533 spots of enhanced biological production.

534

535 The pressure exerted by zooplankton grazers varies seasonally (Fig 9.c .d). It shows a similar
536 seasonal cycle in the LCEs core and in the background GoM. On average, ~ 90% of the total growth is
537 consumed by grazers, reaching the highest impact in March, just one month after the peak season of the
538 PP_{tot} in both areas. In February the difference between the primary production and the grazing rate
539 tends to be larger in the LCEs core ($GRZ_{tot}/PP_{tot} = 0.95 \pm 0.08$) than in the GoM background
540 ($GRZ_{tot}/PP_{tot} = 0.96 \pm 0.13$, Fig. 9.c), leading to an enhanced net primary production. Considering the
541 ecosystem from a “top-down” perspective, the grazing rate also participates then in enhancing $[CHL]_{tot}$
542 within the LCEs core compared to the background.

543

544 **IV.4 Eddy-wind interactions**

545

546 In summer, the total primary production is higher in the background GoM waters as the
547 regenerated production rate is higher. Since grazing is known to be a major contributor of the recycling

548 loop in the euphotic zone (Sherr and Sherr, 2002), the lower grazing rate inside the LCE during
549 summer (Fig. 9.c.d.) likely explains this lower regenerated production. In addition, the biogeochemical
550 consumption of nitrate that foster the production of organic matter occurs in a deeper layer within the
551 LCEs core compared to the background GoM (Fig. B1. e. f.). It is then more likely exported out of the
552 euphotic layer in the form of settling particle, leading to lower remineralization rates in the upper layers
553 to feed regenerated production. More surprising, the new primary production exhibits similar rates in
554 both regions, although NO_3 depletion occurs deeper in the LCEs core. In the absence of a strong
555 enough vertical mixing when the mixed layer is shallow, this apparent mismatch requires an additional
556 mechanism, vertical advection, capable to supply NO_3 to the euphotic layer (Sweeney et al., 2003;
557 McGillicuddy et al., 2015).

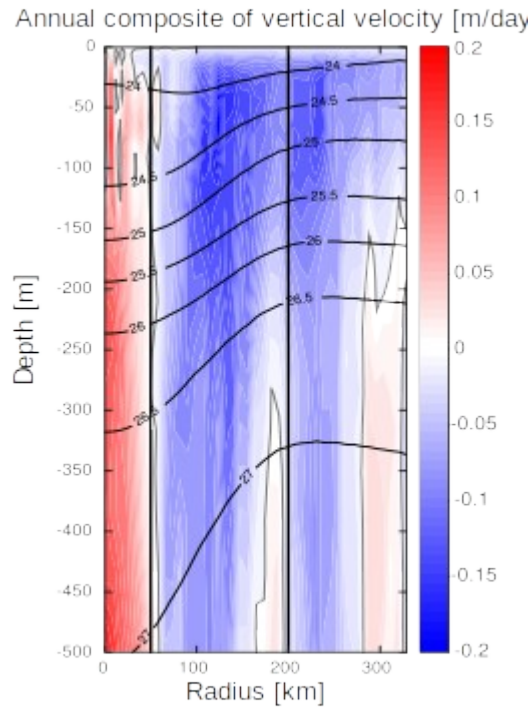
558

559 The model vertical velocity in the LCEs reveals an upward pumping in their core (Fig 11). The
560 vertical velocity between 100 and 500 m is on average $+0.07 \text{ m}\cdot\text{day}^{-1}$. This vertical transport is mainly
561 driven by two mechanisms, eddy pumping (Falkowski et al., 1991) and eddy-wind interaction (Dewar
562 and Flierl, 1987), but their relative importance is difficult to quantify (Gaube et al. 2014; McGillicuddy
563 et al., 2015).

564

565 The eddy pumping mechanism is related to the decay of the rotational velocities from the
566 moment LCEs are released from the Loop Current. In the LCE core, this decay is considered as
567 moderate since lateral diffusivity is expected to be relatively low (section V.1). This process may
568 however be considerable in the LCE ring where the erosion rates are important (Meunier et al., 2020).

569



570 **Figure 11: Annually-averaged LCE composite transects of vertical velocities (m/day). Isopycnals anomalies (black contours) are**
 571 **superimposed on all panels. Vertical white lines delimit the three dynamical fields of the LCE composite.**

572

573 Eddy-wind interactions are due to mesoscale modulation of the Ekman transport, so that they are
 574 often qualified as eddy-Ekman pumping (He et al, 2017). Following the observation of a LCE core in
 575 quasi-solid body rotation, the horizontal vorticity varies little with the radius resulting in a negligible
 576 “non-linear” contribution of the Ekman pumping (McGillicuddy et al., 2008; Gaube et al., 2015).
 577 Assuming a small effect of the eddy SST-induced Ekman pumping, the total Ekman pumping

578 simplifies into its “linear” contribution computed as $W_E = \frac{\nabla \times \tau}{\rho_0 \cdot (f + \zeta)}$, where ρ_0 is the surface density, f
 579 the Coriolis parameter, τ the stress at the sea surface depending on both the wind and ocean currents at
 580 the surface (Martin and Richards, 2001, equation 12) and $\nabla \times$ the curl operator. Considering uniform
 581 wind velocities ranging from 4.5 to 7.5 m·s⁻¹ (Nowlin & Parker, 1974; Passalacqua et al., 2016)
 582 blowing over the LCE, the curl of the stress arises from the anticyclonic surface circulation generated
 583 by the eddy. Its manifestation is a persistent horizontal divergence at surface balanced by an upward

584 pumping in the eddy interior (see Martin & Richards, 2001; Gaube et al., 2013, 2014 for further
585 details). With $\rho_0 \sim 1023 \text{ kg}\cdot\text{m}^{-3}$ and $f \sim 6.2\cdot 10^{-5} \text{ s}^{-1}$, we estimate W_E to range from + 0.06 to $0.13 \text{ m}\cdot\text{day}^{-1}$,
586 in agreement with the modeled vertical velocity within the core. The Ekman-eddy pumping
587 mechanism could explain a large fraction of the gradual upwelling within the eddy's core (Fig. 11) and
588 may actively contribute to the advective vertical flux of nutrients (see Appendix B). In summer, this
589 mechanism could explain why new primary production rates are similar in the LCEs core and the
590 background GoM waters although the nutrient pool is located much deeper in the LCEs core.

591

592 The eddy-Ekman pumping persists in the LCEs core throughout their lifetime as long as there is
593 a wind stress applied at the surface. During wintertime, we expect that both vertical mixing and eddy-
594 Ekman pumping participate to increase the new primary production. A question then arises on the
595 relative contribution of winter mixing to eddy-Ekman pumping in the LCEs core primary production
596 increase in winter. This issue was tackled by He et al. (2017) and Travis et al. (2019) comparing the
597 rate of change of the mixed layer depth with the vertical velocity induced by the eddy-Ekman pumping
598 (equation 4 in He et al, 2017). In the GoM, even if the wind shows larger magnitudes in winter, it is
599 also associated with a large variability. As a consequence, the variability of Ekman pumping is also
600 found large and a robust seasonal cycle which would allow to isolate the Ekman pumping in winter
601 cannot be clearly identified. However, in the LCEs core, we estimate the mixed layer to deepen at
602 roughly $0.8 \text{ m}\cdot\text{day}^{-1}$, which is on average about one order of magnitude larger than the higher bound of
603 the estimated pumping mechanism typically occurring in winter in response to stronger wind events.
604 This supports winter mixing as the overwhelming process for the LCEs-induced primary production
605 peak in winter.

606

607 **V/ Summary and perspectives**

608

609 The [CHL] variability induced by the mesoscale Loop Current Eddies in the Gulf of Mexico is
610 studied by analyzing vortex composite fields generated from a coupled physical-biogeochemical model
611 at 1/12° horizontal resolution. LCEs are hotspots for mesoscale biogeochemical variability. Despite the
612 [CHL]_{surf} negative anomaly associated with their core ($r < 50$ km), model results indicate that LCEs are
613 associated with enhanced phytoplankton biomass content, particularly in winter. This enhancement
614 results from the contribution of multiple mechanisms of physical-biogeochemical interactions and
615 contrasts with the background oligotrophic surface waters of the GoM.

616

617 The main results of this study are:

- 618 • LCEs cores present a negative surface chlorophyll anomaly,
- 619 • Unlike [CHL]_{surf}, [CHL]_{tot} is larger in the LCEs cores compared to the background GoM in
620 winter.
- 621 • LCEs core trigger a large phytoplankton biomass increase in winter,
- 622 • The winter mixing is a key mesoscale mechanism that preferentially supplies nutrients to the
623 euphotic layer within the LCEs core. Consequently, it drives an eddy-induced peak of new
624 primary production,
- 625 • Ekman-eddy pumping is a significant mechanism for sustaining relatively high new primary
626 production rates within LCE cores during summer.

627 The phytoplankton biomass increase in individual LCEs cores suggests that LCEs play an important
628 role in sustaining the large-scale GoM productivity.

629

630 GOLFO12-PISCES provides numerical results which were largely confronted to observations.
631 This extensive validation gives confidence about its ability to produce realistic seasonal and mesoscale
632 variability of biogeochemical tracers at surface and sub-surface, in particular the one associated with

633 LCEs. However, biases are inherent to model and might affect the main conclusions drawn. For
634 example, in-situ measurements reveal an intense variability of [CHL] vertical profiles in winter that the
635 model tends to underestimate (Green et al., 2014; Damien et al., 2018). In particular, some individual
636 observed profiles in winter present a DCM while GOLFO12-PISCES largely favors well mixed [CHL]
637 profiles. The under-representation of these profiles, potentially due to a relatively coarse model
638 resolution, could be associated with an under-estimation of [CHL]_{tot} in winter. The results exposed in
639 this study would require further confirmation, notably by more sub-surface in-situ measurements, in
640 particular within the core of LCEs where no [CHL] profiles were observed in winter.

641

642 Although the biological response to LCEs may present some specificities due to the particular
643 dynamical nature of LCEs, this study suggests potentially generic insights on the biogeochemical role
644 that anticyclonic eddies could play in oligotrophic environments. It echoes the previous works of
645 Martin and Richards (2001), Gaube et al. (2014, 2015) and especially Dufois et al. (2014, 2016) and He
646 et al. (2017) who proposed winter vertical mixing as an explanation for the positive [CHL]_{surf} anomaly
647 observed in anticyclones in the South Indian Ocean. One of the most crucial points to be underlined
648 from our results is that the enhanced primary production and biomass content within anticyclonic
649 eddies may not necessarily be correlated with the surface layer variability. In oligotrophic areas, the
650 integrated content of chlorophyll in the water column has to be considered. This implies that caution
651 should be exercised in the analysis and interpretation of [CHL]_{surf} observed by remote sensing
652 instruments and highlights the crucial need for in-situ biogeochemical and bio-optical measurements.
653 In oligotrophic environments, defined by their low production rates and their low chlorophyll
654 concentration, anticyclonic eddies are able to trigger local enhanced biological productivity and
655 generate phytoplankton biomass positive anomalies. In a scenario of expansion of oligotrophic areas
656 (Barnett et al., 2001; Behrenfeld et al., 2006; Polovina et al., 2008), the fate and role of mesoscale
657 anticyclones is an important aspect to be considered.

658

659 This study focuses on mesoscale physical-biogeochemical interactions which is the spectral
660 range resolved by GOLFO12-PISCES configuration. It evidences the important role of mixing on
661 primary production in the LCE core at seasonal scale. However, mixing also presents significant
662 fluctuations at higher frequencies, associated with particular atmospheric events like storms. The PP_{tot}
663 response to such forcing requires further investigation to verify if the correlation between PP_{tot} and
664 mixing still hold on at higher frequencies where additional other drivers might also become important.
665 For instance, the role of submesoscale is of particular interest since it has been proved to trigger
666 mechanisms of significance importance for biogeochemistry (Levy et al., 2018). Higher model
667 resolutions can locally enhanced density gradients (Levy et al., 2012; Omand et al., 2015) leading to
668 ageostrophic circulations that perturbs the circular flow around vortices (Martin and Richards, 2001) or
669 enhanced vertical velocities that potentially foster the nutrient supply to the euphotic layer. Beside the
670 mesoscale Ekman pumping located at the eddy center, eddy-wind interactions also produce vertical
671 velocities at the eddy periphery (e.g. Flierl and McGillicuddy, 2002). Finally, it is also worth noting
672 that anticyclonic mesoscales eddies are capable of trapping near-inertial energy waves in the ocean
673 (Kunze 1985, Danioux et al. 2008, Koszalka et al. 2010, Pallas-Sanz et al., 2016) where they produce
674 vertical recirculation patterns (Zhong and Bracco, 2013). Even if, some of these dynamical aspects are
675 partially resolved at $1/12^\circ$ horizontal resolution, higher resolutions simulations with higher frequency
676 outputs are necessary to correctly assess their specific impact.

677

678

679

680 **Acknowledgments:** Funding for this study comes from the National Council of Science and
681 Technology of Mexico (CONACYT) -Mexican Ministry of Energy (SENER) Hydrocarbon Trust,
682 project 201441 and a contribution of the Gulf of Mexico Research Consortium (CIGoM), We

683 acknowledge PEMEX's specific request to the Hydrocarbon Fund to address the environmental effects
684 of oil spills in the Gulf of Mexico. We acknowledge the provision of supercomputing facilities by
685 CICESE.

686

687

688 **APPENDIX A: CHL/C-biomass ratio and ecosystem structure**

689

690 [CHL] is widely used as a proxy for photosynthetic biomass (Strickland, 1965; Cullen, 1982).
691 However, in addition to depend on phytoplankton concentration, it is also affected by several other
692 factors mainly produced by intracellular physiological mechanisms (Geider, 1987). In particular,
693 photoacclimation processes have been proved to be determinant to explain [CHL]_{surf} variability in
694 oligotrophic areas (Mignot et al. 2014). In the GoM open-waters, this issue was specifically addressed
695 at a basin scale in Pasqueron de Fommervault et al. (2017) considering in-situ particulate
696 backscattering measurements and in Damien et al. (2018) from modeling tools. They both reach the
697 same conclusion: [CHL]_{tot} variability provides a reasonably good estimate of the total C-biomass
698 variability ([PHY]_{tot}).

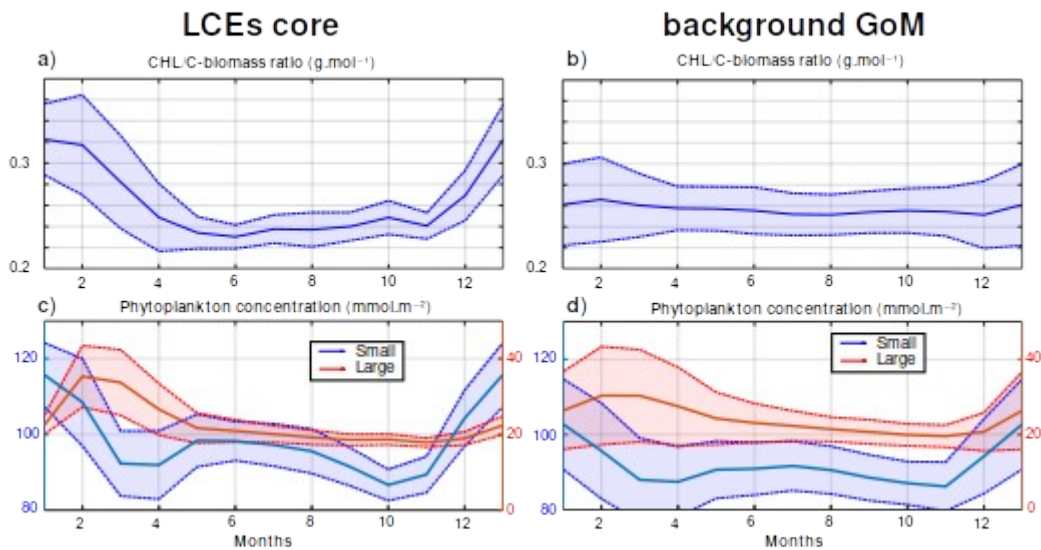
699

700 This is confirmed by the small amplitude of the seasonal cycle of the ratio [CHL]_{tot}/[PHY]_{tot} in
701 the background GoM (0.256 +/- 0.004 g·mol⁻¹ averaged throughout the year, Fig A1). In the LCEs
702 core, this statement is still valid but must be qualified, since the ratio [CHL]_{tot}/[PHY]_{tot} presents small
703 but significant changes through the year (Fig A1.a). It is around 0.24 g·mol⁻¹ from March to November
704 and increases sharply in December to reach about 0.32 g·mol⁻¹ in January and February. As a result, in
705 winter, the photoacclimation mechanism accounts for ~25% of the total [CHL]_{tot} increase (the
706 remaining part being an effective phytoplankton biomass increase). In summer, the ratio
707 [CHL]_{tot}/[PHY]_{tot} is slightly lower in the LCEs core compared to the background GoM. As a
708 consequence, the [CHL]_{tot} negative anomaly associated with LCEs core does not necessarily translate
709 into a [PHY]_{tot} negative anomaly.

710

711 Overall in the GoM open-waters, there is a dominance of the small-size phytoplankton over the
712 large-size class in proportion closed to 80%:20% (Linacre et al., 2015). Although the modeled

713 ecosystem structure is relatively simple, this typical community size structure is well reproduced by
 714 GOLFO12-PISCES (Fig A1.c and A1.d), that also suggests a shift in the ecosystem structure in winter.
 715 The different response among size classes results from the enhancement of nutrient vertical flux. The
 716 role of “secondary” nutrient in this change in the community composition must not be overlooked also,
 717 in particular for diatoms (accounted in the model’s large-size group) since they also uptake on silicate
 718 (Benitez-Nelson et al., 2007). Moreover, GOLFO12-PISCES exhibits a modulation of the ecosystem
 719 structure by LCEs. The dominance of small-size phytoplankton is slightly more marked in summer and
 720 the winter shift is stronger in the LCEs core.
 721



722 **Figure A1: Climatological seasonal cycles of (a and b) the CHL/C-biomass ratio and (c and d) the vertically integrated content of**
 723 **phytoplankton concentration (small size in blue, large size in red). The left panels (a and c) refer to the time series in the LCEs**
 724 **core ($r < 50$ km) whereas the right panels (b and d) refer to the time series in the background GoM ($r > 200$ km). For each**
 725 **average cycle, the average value is shown (full line) along with its variability (± 1 standard deviation relative to the mean, dashed**
 726 **lines).**

728

729 **APPENDIX B : Nitrate budget at a seasonal scale**

730

731 Nutrients availability in the euphotic layer is a key mechanism to trigger biomass increase in
 732 LCEs. The processes driving the seasonality of nutrient concentrations are here investigated diagnosing
 733 the different contributions to nitrate concentrations (hereafter [NO₃]) variability. The goal is to confirm
 734 the vertical transport of nutrients and quantify the budget in order to determine the driving mechanisms.
 735 The analysis is restricted to nitrate concentrations, considered as the main limiting factor for large size-
 736 class phytoplankton growth in the GoM (Myers et al., 1981; Turner et al., 2006), although phosphates
 737 and silicates are also modeled. We do not exclude that phosphates or silicates could also play a
 738 significant role. In cylindrical coordinates, the [NO₃] equation reads:

$$\frac{\partial NO_3}{\partial t} = \underbrace{-V_r \frac{\partial NO_3}{\partial r}}_{\text{radial advection}} - \underbrace{\frac{V_\theta}{r} \frac{\partial NO_3}{\partial \theta}}_{\text{azimuthal advection}} - \underbrace{V_z \frac{\partial NO_3}{\partial z}}_{\text{vertical advection}} + \underbrace{\frac{D_l}{r} \frac{\partial}{\partial r} \left(r \frac{\partial NO_3}{\partial r} \right) + \frac{D_l}{r^2} \frac{\partial^2 NO_3}{\partial \theta^2}}_{\text{lateral diffusion}} + \underbrace{\frac{\partial}{\partial z} \left(K_z \frac{\partial NO_3}{\partial z} \right)}_{\text{vertical diffusion}} + \underbrace{\text{SMS}}_{\text{Source minus sink}} + \text{Asselin}$$

739

740 Basically, this is a 3D advection-diffusion equation with added "sources and sinks" terms, namely
 741 biogeochemical release and uptake rates. One must include also an "Asselin term", a modeling artifact
 742 due to the Asselin time filtering. We focus on the seasonal cycle of three particular trend terms: the
 743 vertical mixing (Fig B1.a and B1.b), the vertical advection (Fig B1.c and B1.d) and a "source minus
 744 sink" term (Fig B1.e B1.f).

745

746 [NO₃] variations from vertical dynamics are mainly positive, especially in the first 100 m of the
 747 water column. This traduces in year-round NO₃ source driven by physical processes. By contrast,
 748 biogeochemical processes consume NO₃ in the upper layer to sustain the primary production (Fig B1.e
 749 and B1.f). In the sub-surface layer (~ below the isoline on which nitrate concentration is equal to 2
 750 mmol.m⁻³), the process of nitrification constitutes a biological source of [NO₃]. To first order, this

751 represents the global functioning of the ecosystem, valid in both fields and throughout the year.

752 However, the seasonal cycle strongly influence the magnitude of these trend terms, in particular in the
753 LCE core.

754

755 In winter, from December to February, vertical advective and diffusive motions produce an
756 increase of $[\text{NO}_3]$ within the mixed layer. This tendency consists in an advective entrainment resulting
757 from the deepening of the mixed layer which mainly acts to increase $[\text{NO}_3]$ at the base of the mixed
758 layer (Fig B1.c and B1.d) and vertical mixing which redistributes vertically the nutrients and tends to
759 homogenize $[\text{NO}_3]$ in the mixed layer (Fig B1.a and B1.b). The winter $[\text{NO}_3]$ increase is most important
760 in the LCE core at the base of the mixed layer ($\sim + 6.5 \cdot 10^{-7} \text{ mmol} \cdot \text{m}^{-3} \cdot \text{d}^{-1}$, nearly 3 times larger than in
761 the background GoM), attesting here a preferential NO_3 uplift due to deeper convection. Integrated
762 over the mixed layer, the winter vertical fluxes produce $[\text{NO}_3]$ enhancement of $\sim 2.4 \cdot 10^{-5} \text{ mmol} \cdot \text{m}^{-2} \cdot \text{d}^{-1}$
763 in the eddy core whereas it is only of $\sim 1.6 \cdot 10^{-5} \text{ mmol} \cdot \text{m}^{-2} \cdot \text{d}^{-1}$ in the background GoM. This also
764 explains why, on average, the density/nitrate relation differs in the LCEs core (Fig 5.e). In response, the
765 $[\text{NO}_3]$ tendency due to biogeochemical processes indicates an increase of the $[\text{NO}_3]$ uptake. This
766 increase is about 1.5 times larger in the core ($\sim - 1.3 \cdot 10^{-3} \text{ mmol} \cdot \text{m}^{-2} \cdot \text{d}^{-1}$ integrated over the mixed layer)
767 than in the background GoM ($\sim - 0.9 \cdot 10^{-3} \text{ mmol} \cdot \text{m}^{-2} \cdot \text{d}^{-1}$). Knowing that it feeds biomass production, this
768 $[\text{NO}_3]$ loss is consistent with the primary production peak in winter (Fig 9.e and 9.f).

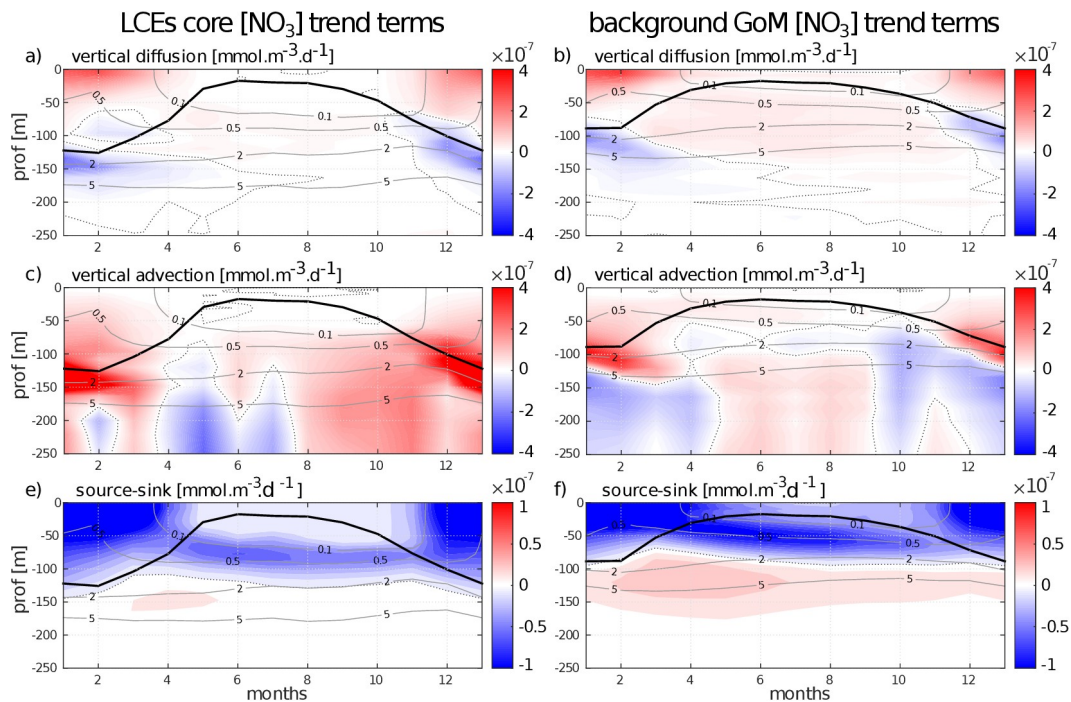
769

770 In summer, $[\text{NO}_3]$ variations due to vertical processes are smaller than in winter. They are also
771 weaker in the LCEs core upper layer (almost nil in the 0-50m layer) compared to the background GoM,
772 consistent with a deeper NO_3 pool and a shallow mixer layer. In the eddy core, one can assume that the
773 NO_3 vertical supply is entirely consumed before reaching 50m. Below 50m, vertical $[\text{NO}_3]$ diffusive
774 trends are consistently more important in the background GoM, in agreement with a steeper nitracline
775 (Fig 5.e). In contrast, vertical $[\text{NO}_3]$ advective trends in the eddy core are similar to or can eventually

776 exceed the trends in the background GoM (as in September and October for example). This confirms a
 777 pumping mechanism to sustain primary production in summer within the eddy core (section V.4) The
 778 biogeochemical activity related to $[\text{NO}_3]$ variations is also less intense in summer compared to winter.
 779 The depth of maximum $[\text{NO}_3]$ uptake is located just above the DCM and $[\text{NO}_3]$ release below. The loss
 780 of $[\text{NO}_3]$ is about twice larger in the background GoM ($\sim -0.9 \cdot 10^{-7} \text{ mmol} \cdot \text{m}^{-3} \cdot \text{d}^{-1}$) than in the LCEs core
 781 ($\sim -0.5 \cdot 10^{-7} \text{ mmol} \cdot \text{m}^{-3} \cdot \text{d}^{-1}$). It is noteworthy that the biogeochemical $[\text{NO}_3]$ source term, namely the
 782 nitrification rate, is really low within the eddy core.

783

784 To close this analysis of the $[\text{NO}_3]$ budget, it must be said that lateral diffusion and Asselin
 785 tendencies are marginal terms compared to the others. Horizontal advection is of the same order of
 786 magnitude as the vertical terms and mainly acts to redistribute horizontally the NO_3 vertically moved
 787 (see supplementary material 1).



788 **Figure B1: Seasonal cycle of nitrate trend terms in the (left column) LCEs core and in the (right column) background GoM. The**
 789 **trend induced by (a and b) vertical mixing, the (c and d) vertical advection and the (e and f) biogeochemical source minus sink are**
 790 **represented. Isopycnals anomalies (gray contours) and the depth of the mixed layer (black line) are superimposed.**

791 **REFERENCES:**

792

793 Ascani, F., Richards, K. J., Firing, E., Grant, S., Johnson, K. S., Jia, Y., et al. (2013). Physical and
794 biological controls of nitrate concentrations in the upper subtropical North Pacific Ocean. *Deep Sea*
795 *Research, Part II*, 93, 119–134.

796

797 Aumont, O., & Bopp, L. (2006). Globalizing results from ocean in situ iron fertilization studies. *Global*
798 *Biogeochemical Cycles*, 20, GB2017. <https://doi.org/10.1029/2005GB002591>.

799

800 Aumont, O., Ethé, C., Tagliabue, A., Bopp, L., & Gehlen, M. (2015). PISCES-v2: An ocean
801 biogeochemical model for carbon and ecosystem studies. *Geoscientific Model Development*, 8(8),
802 2465–2513.

803

804 Badan Jr, A., Candela, J., Sheinbaum, J., & Ochoa, J. (2005). Upper-layer circulation in the approaches
805 to Yucatan Channel. *Washington DC American Geophysical Union Geophysical Monograph*
806 *Series*, 161, 57-69.

807

808 Barnett, T. P., Pierce, D. W., & Schnur, R. (2001). Detection of anthropogenic climate change in the
809 world's oceans. *Science*, 292(5515), 270-274.

810

811 Behrenfeld, M. J., O'Malley, R. T., Siegel, D. A., McClain, C. R., Sarmiento, J. L., Feldman, G. C., ...
812 & Boss, E. S. (2006). Climate-driven trends in contemporary ocean productivity. *Nature*, 444(7120),
813 752.

814

815 Benitez-Nelson, C. R., Bidigare, R. R., Dickey, T. D., Landry, M. R., Leonard, C. L., Brown, S. L., ...
816 & Bibby, T. S. (2007). Mesoscale eddies drive increased silica export in the subtropical Pacific Ocean.
817 *Science*, 316(5827), 1017-1021.

818

819 Biggs, D. C., & Ressler, P. H. (2001). Distribution and abundance of phytoplankton, zooplankton,
820 ichthyoplankton, and micronekton in the deepwater Gulf of Mexico. *Gulf of Mexico Science*, 19(1), 2.

821

822 Bracco, A., Provenzale, A., & Scheuring, I. (2000). Mesoscale vortices and the paradox of the
823 plankton. *Proceedings of the Royal Society of London B: Biological Sciences*, 267(1454), 1795-1800.

824

825 Brodeau, L., Barnier, B., Treguier, A.-M., Penduff, T., & Gulev, S. (2010). An ERA40-based
826 atmospheric forcing for global ocean circulation models. *Ocean Modelling*, 31, 88–104.
827 <https://doi.org/10.1016/j.ocemod.2009.10.005>

828

829 Brokaw, R. J., Subrahmanyam, B., & Morey, S. L. (2019), Loop current and eddy driven salinity
830 variability in the Gulf of Mexico, *Geophysical Research Letters*, 46, 5978–5986,
831 <https://doi.org/10.1029/2019GL082931>.

832

833 Chelton, D., DeSzoek, R., Schlax, M., El Naggar, K., & Siwertz, N. (1998). Geographical variability
834 of the first baroclinic Rossby radius of deformation. *Journal of Physical Oceanography*, 28(3), 433–
835 460.

836

837 Ciani, D., Carton, X., Aguiar, A. B., Peliz, A., Bashmachnikov, I., Ienna, F., ... & Santoleri, R. (2017).
838 Surface signature of Mediterranean water eddies in a long-term high-resolution simulation. *Deep Sea*
839 *Research Part I: Oceanographic Research Papers*, 130, 12-29.

840

841 Cooper, C., Forristall, G. Z., & Joyce, T. M. (1990). Velocity and hydrographic structure of two Gulf of
842 Mexico warm-core rings. *Journal of Geophysical Research: Oceans*, 95(C2), 1663-1679.

843

844 Cullen, J. J. (1982). The deep chlorophyll maximum: Comparing vertical profiles of chlorophyll a.
845 *Canadian Journal of Fisheries and Aquatic Sciences*, 39(5), 791–803.

846

847 Dai, A., & Trenberth, K. E. (2002). Estimates of freshwater discharge from continents: Latitudinal and
848 seasonal variations. *Journal of Hydro-meteorology*, 3, 660–687.

849

850 Damien, P., Pasqueron de Fommervault, O., Sheinbaum, J., Jouanno, J., Camacho-Ibar, V. F., &
851 Duteil, O. (2018). Partitioning of the Open Waters of the Gulf of Mexico Based on the Seasonal and
852 Interannual Variability of Chlorophyll Concentration. *Journal of Geophysical Research: Oceans*.

853

854 Danioux, E., Klein, P., & Rivière, P. (2008). Propagation of wind energy into the deep ocean through a
855 fully turbulent mesoscale eddy field. *Journal of Physical Oceanography*, 38(10), 2224-2241.

856

857 Dewar, W., and G. Flierl (1987), Some effects of the wind on rings, *J. Phys. Oceanogr.*, 17(10), 1653–
858 1667.

859

860 Doney, S. C., Glover, D. M., McCue, S. J., & Fuentes, M. (2003). Mesoscale variability of Sea-viewing
861 Wide Field-of-view Sensor (SeaWiFS) satellite ocean color: Global patterns and spatial scales. *Journal*
862 *of Geophysical Research: Oceans*, 108(C2).

863

864 Dong, C., X. Lin, Y. Liu, F. Nencioli, Y. Chao, Y. Guan, D. Chen, T. Dickey, and J. C. McWilliams
865 (2012), Three-dimensional oceanic eddy analysis in the Southern California Bight from a numerical
866 product, *J. Geophys. Res.*, 117, C00H14, doi:10.1029/2011JC007354.

867

868 Donohue, Kathleen A., et al. "Loop current eddy formation and baroclinic instability." *Dynamics of*
869 *Atmospheres and Oceans* 76 (2016): 195-216.

870

871 d'Ovidio, F., De Monte, S., Della Penna, A., Cotté, C., & Guinet, C. (2013). Ecological implications of
872 eddy retention in the open ocean: a Lagrangian approach. *Journal of Physics A: Mathematical and*
873 *Theoretical*, 46(25), 254023.

874

875 Dufois, F., Hardman-Mountford, N. J., Greenwood, J., Richardson, A. J., Feng, M., Herbette, S., &
876 Matear, R. (2014). Impact of eddies on surface chlorophyll in the South Indian Ocean. *Journal of*
877 *Geophysical Research: Oceans*, 119(11), 8061-8077.

878

879 Dufois, F., Hardman-Mountford, N. J., Greenwood, J., Richardson, A. J., Feng, M., & Matear, R. J.
880 (2016). Anticyclonic eddies are more productive than cyclonic eddies in subtropical gyres because of
881 winter mixing. *Science advances*, 2(5), e1600282.

882

883 Dufois, F., Hardman-Mountford, N. J., Fernandes, M., Wojtasiewicz, B., Shenoy, D., Slawinski, D., ...
884 & Toresen, R. (2017). Observational insights into chlorophyll distributions of subtropical South Indian
885 Ocean eddies. *Geophysical Research Letters*, 44(7), 3255-3264.

886

887 Dugdale, R. C., and J. J. Goering (1967), Uptake of new and regenerated forms of nitrogen in primary
888 productivity, *Limnol. Oceanogr.*, 12, 196–206

889

890 Early, J. J., Samelson, R. M., & Chelton, D. B. (2011). The evolution and propagation of
891 quasigeostrophic ocean eddies. *Journal of Physical Oceanography*, 41(8), 1535-1555.

892

893 Elliott, B. A. (1982). Anticyclonic rings in the Gulf of Mexico. *Journal of Physical Oceanography*,
894 12(11), 1292-1309.

895

896 Eppley, R. W., and B. J. Peterson (1979), Particulate organic matter flux and planktonic new
897 production in the deep ocean, *Nature*, 282, 677–680.

898

899 Falkowski, P., D. Ziemann, Z. Kolber, and P. Bienfang (1991), Role of eddy pumping in enhancing
900 primary production in the ocean, *Nature*, 352(6330), 55–58.

901

902 Flierl, G. R. (1981). Particle motions in large-amplitude wave fields. *Geophysical & Astrophysical*
903 *Fluid Dynamics*, 18(1-2), 39-74.

904

905 Flierl, G. R., & McGillicuddy, D. J. (2002). Mesoscale and submesoscale physical-biological
906 interactions. *The sea*, 12, 113-185.

907

908 de Fommervault, O. P., Perez-Brunius, P., Damien, P., Camacho-Ibar, V. F., & Sheinbaum, J. (2017).
909 Temporal variability of chlorophyll distribution in the Gulf of Mexico: bio-optical data from profiling
910 floats. *Biogeosciences*, 14(24), 5647.

911

912 Forristall, G. Z., Schaudt, K. J., & Cooper, C. K. (1992). Evolution and kinematics of a Loop Current
913 eddy in the Gulf of Mexico during 1985. *Journal of Geophysical Research: Oceans*, 97(C2), 2173-
914 2184.

915

916 Frolov, S. A., et al. "Loop Current eddy interaction with the western boundary in the Gulf of Mexico."
917 *Journal of physical oceanography* 34.10 (2004): 2223-2237.

918

919 Garcia, H. E., Locarnini, R. A., Boyer, T. P., Antonov, J. I., Baranova, O. K., Zweng, M. M., et al.
920 (2010). World Ocean Atlas 2009. In S. Levitus (Ed.), Dissolved oxygen, apparent oxygen utilization,
921 and oxygen saturation (NOAA Atlas NESDIS 70, Vol. 3, 344 p.). Washington, DC: U.S. Government.
922 Printing Office.

923

924 Garcia-Jove Navarro, M., Sheinbaum Pardo, J., & Jouanno, J. (2016). Sensitivity of Loop Current
925 metrics and eddy detachments to different model configurations: The impact of topography and
926 Caribbean perturbations. *Atmosfera*, 29(3), 235–265. <https://doi.org/10.20937/ATM.2016.29.03.05>

927

928 Garçon, V. C., Oschlies, A., Doney, S. C., McGillicuddy, D., & Waniek, J. (2001). The role of
929 mesoscale variability on plankton dynamics in the North Atlantic. *Deep Sea Research Part II: Topical*
930 *Studies in Oceanography*, 48(10), 2199-2226.

931

932 Gaube, P., Chelton, D. B., Strutton, P. G., & Behrenfeld, M. J. (2013). Satellite observations of
933 chlorophyll, phytoplankton biomass, and Ekman pumping in nonlinear mesoscale eddies. *Journal of*
934 *Geophysical Research: Oceans*, 118(12), 6349-6370.

935

936 Gaube, P., McGillicuddy, D. J., Chelton, D. B., Behrenfeld, M. J., & Strutton, P. G. (2014). Regional
937 variations in the influence of mesoscale eddies on near-surface chlorophyll. *Journal of Geophysical*
938 *Research: Oceans*, 119(12), 8195-8220.

939

940 Gaube, P., Chelton, D. B., Samelson, R. M., Schlax, M. G., & O'Neill, L. W. (2015). Satellite
941 observations of mesoscale eddy-induced Ekman pumping. *Journal of Physical Oceanography*, 45(1),
942 104-132.

943

944 Geider, R. J. (1987), Light and temperature dependence of the carbon to chlorophyll a ratio in
945 microalgae and cyanobacteria: implications for physiology and growth of phytoplankton, *New Phytol.*,
946 106, 1–34.

947

948 Geider, R. J., MacIntyre, H. L., & Kana, T. M. (1997). A dynamical model of phytoplankton growth
949 and acclimation: Response of the balanced growth rate to light, nutrient limitation and temperature.
950 *Marine Ecology Progress Series*, 148, 187–200.

951

952 Glenn, S. M., and C. C. Ebbesmeyer (1993), Drifting buoy observations of a loop current
953 anticyclonic eddy, *J. Geophys. Res.*, , 98, 20, doi:10.1029/93JC02078.

954

955 Green, R. E., Bower, A. S., & Lugo-Fernández, A. (2014). First autonomous bio-optical profiling float
956 in the Gulf of Mexico reveals dynamic biogeochemistry in deep waters. *PloS one*, 9(7), e101658.

957

958 Guo, M., P. Xiu, S. Li, F. Chai, H. Xue, K. Zhou, and M. Dai (2017), Seasonal variability and
959 mechanisms regulating chlorophyll distribution in mesoscale eddies in the South China Sea, *J.*
960 *Geophys. Res. Oceans*, 122, 5329–5347, doi:10.1002/2016JC012670.

961

962 Hamilton, P., Leben, R., Bower, A., Furey, H., & Pérez-Brunius, P. (2018). Hydrography of the Gulf of
963 Mexico Using Autonomous Floats. *Journal of Physical Oceanography*, 48(4), 773-794. DOI:
964 10.1175/JPO-D-17-0205.1

965

966 Hamilton, P. (2007). Eddy statistics from Lagrangian drifters and hydrography for the northern Gulf of
967 Mexico slope. *Journal of Geophysical Research*, 112, C09002. <https://doi.org/10.1029/2006JC003988>

968

969 He, Q., Zhan, H., Shuai, Y., Cai, S., Li, Q. P., Huang, G., & Li, J. (2017). Phytoplankton bloom
970 triggered by an anticyclonic eddy: The combined effect of eddy Ekman pumping and winter mixing.
971 *Journal of Geophysical Research: Oceans*, 122(6), 4886-4901.

972

973 Hernandez-Guerra, A., & Joyce, T. M. (2000). Water masses and circulation in the surface layers of the
974 Caribbean at 66 W. *Geophysical Research Letters*, 27(21), 3497–3500.
975 <https://doi.org/10.1029/1999GL011230>

976

977 Herrmann, M., Somot, S., Sevault, F., Estournel, C., & Deque, M. (2008). Modeling the deep
978 convection in the northwestern Mediterranean Sea using an eddy-permitting and an eddy-resolving
979 model: Case study of winter 1986–1987. *Journal of Geophysical Research*, 113, C04011.
980 <https://doi.org/10.1029/2006JC003991>

981

982 Huang, J., & Xu, F. (2018). Observational evidence of subsurface chlorophyll response to mesoscale
983 eddies in the North Pacific. *Geophysical Research Letters*, 45, 8462–8470.

984 <https://doi.org/10.1029/2018GL078408>

985

986 Jolliff, J. K., Kindle, J. C., Penta, B., Helber, R., Lee, Z., Shulman, I., Arnone, R., and Rowley, C. D.,
987 (2008). On the relationship between satellite-estimated bio-optical and thermal properties in the Gulf of
988 Mexico, *J. Geophys. Res.*, 113, G1, <https://doi.org/10.1029/2006JG000373>
989

990 Jouanno, J., Ochoa de la Torre, J. L., Pallas Sanz, E., Sheinbaum Pardo, J., Andrade Canto, F., Candela
991 Perez, J., et al. (2016). Loop current frontal eddies: Formation along the Campeche Bank and impact of
992 coastally trapped waves. *Journal of Physical Oceanography*, 46(11), 3339–3363.
993 <https://doi.org/10.1175/JPO-D-16-0052.1>
994

995 Klein, P., & Lapeyre, G. (2009). The oceanic vertical pump induced by mesoscale and submesoscale
996 turbulence. *Annual review of marine science*, 1, 351-375.
997

998 Koszalka, I. M., Ceballos, L., & Bracco, A. (2010). Vertical mixing and coherent anticyclones in the
999 ocean: the role of stratification. *Nonlinear Processes in Geophysics*, 17(1), 37-47.
1000

1001 Kouketsu, S., Tomita, H., Oka, E., Hosoda, S., Kobayashi, T., & Sato, K. (2011). The role of meso-
1002 scale eddies in mixed layer deepening and mode water formation in the western North Pacific. In *New*
1003 *Developments in Mode-Water Research* (pp. 59-73). Springer, Tokyo.
1004

1005 Kunze, E. (1985). Near-inertial wave propagation in geostrophic shear. *Journal of Physical*
1006 *Oceanography*, 15(5), 544-565.
1007

1008 Lascaratos, A., & Nittis, K. (1998). A high-resolution three-dimensional numerical study of
1009 intermediate water formation in the Levantine Sea. *Journal of Geophysical Research*, 103(C9), 18497–
1010 18511.

1011

1012 Lehahn, Y., F. d'Ovidio, M. Levy, Y. Amitai, and E. Heifetz (2011), Long range transport of a quasi
1013 isolated chlorophyll patch by an Agulhas ring, *Geophys. Res. Lett.*, 38, L16610,
1014 doi:10.1029/2011GL048588.

1015

1016 Le Hénaff, M., Kourafalou, V. H., Morel, Y., & Srinivasan, A. (2012). Simulating the dynamics and
1017 intensification of cyclonic Loop Current Frontal Eddies in the Gulf of Mexico. *Journal of Geophysical*
1018 *Research: Oceans*, 117(C2).

1019

1020 Levitus, S. (1982). Climatological atlas of the world ocean (NOAA Prof. Pap. 13, 173 p.). Washington,
1021 DC: U.S. Government Printing Office.

1022

1023 Lévy, M., Ferrari, R., Franks, P. J., Martin, A. P., & Rivière, P. (2012). Bringing physics to life at the
1024 submesoscale. *Geophysical Research Letters*, 39(14).

1025

1026 Lévy, M., Franks, P.J.S. & Smith, K.S. (2018). The role of submesoscale currents in structuring marine
1027 ecosystems. *Nat. Commun.*, **9**, 4758

1028

1029 Linacre, L., Lara-Lara, R., Camacho-Ibar, V., Herguera, J. C., Bazán-Guzmán, C., & Ferreira-Bartrina,
1030 V. (2015). Distribution pattern of picoplankton carbon biomass linked to mesoscale dynamics in the
1031 southern gulf of Mexico during winter conditions. *Deep Sea Research Part I: Oceanographic Research*
1032 *Papers*, 106, 55-67.

1033

1034 Linacre, L., Durazo, R., Camacho-Ibar, V. F., Selph, K. E., Lara-Lara, J. R., Mirabal-Gómez, U., ... &
1035 Sidón-Ceseña, K. (2019). Picoplankton Carbon Biomass Assessments and Distribution of

1036 Prochlorococcus Ecotypes Linked to Loop Current Eddies During Summer in the Southern Gulf of
1037 Mexico. *Journal of Geophysical Research: Oceans*, 124(11), 8342-8359.

1038

1039

1040 Lipphardt, B., Poje, A. C., Kirwan, A., Kantha, L., & Zweng, M. (2008). Death of three Loop Current
1041 rings. *Journal of Marine Research*, 66(1), 25-60.

1042

1043 Madec, G. (2016). NEMO ocean engine, Note Du Pole De Mod# elisation (Vol. 27, 406 p.). Paris,
1044 France: Institut Pierre-Simon Laplace.

1045

1046 Mann, K. H., & Lazier, J. R. N. (2006). Dynamics of marine ecosystems (3rd ed.). Oxford, UK:
1047 Blackwell Publishing.

1048

1049 Mahadevan, A. (2014). Ocean science: Eddy effects on biogeochemistry. *Nature*, 506(7487), 168.

1050

1051 Martin, A. P., & Richards, K. J. (2001). Mechanisms for vertical nutrient transport within a North
1052 Atlantic mesoscale eddy. *Deep Sea Research Part II: Topical Studies in Oceanography*, 48(4-5), 757-
1053 773.

1054

1055 Mayot, N., D'Ortenzio, F., Taillandier, V., Prieur, L., de Fommervault, O. P., Claustre, H., ... & Conan,
1056 P. (2017). Physical and biogeochemical controls of the phytoplankton blooms in North Western
1057 Mediterranean Sea: A multiplatform approach over a complete annual cycle (2012–2013 DEWEX
1058 experiment). *Journal of Geophysical Research: Oceans*, 122(12), 9999-10019.

1059

1060 McClain, C. R., Signorini, S. R., & Christian, J. R. (2004). Subtropical gyre variability observed by
1061 ocean-color satellites. *Deep Sea Research Part II: Topical Studies in Oceanography*, 51(1-3), 281-301.
1062

1063 McGillicuddy, D. J., Jr. (2016), Mechanisms of Physical-Biological-Biogeochemical Interaction at the
1064 Oceanic Mesoscale, *Annu. Rev. Mar. Sci.*, 8, 125–159, doi:10.1146/annurev-marine-010814-015606.
1065

1066 McGillicuddy Jr, D. J., Robinson, A. R., Siegel, D. A., Jannasch, H. W., Johnson, R., Dickey, T. D., ...
1067 & Knap, A. H. (1998). Influence of mesoscale eddies on new production in the Sargasso Sea. *Nature*,
1068 394(6690), 263.
1069

1070 McGillicuddy Jr, D. J., & Robinson, A. R. (1997). Eddy-induced nutrient supply and new production in
1071 the Sargasso Sea. *Deep Sea Research Part I: Oceanographic Research Papers*, 44(8), 1427-1450.
1072

1073 Meunier, T., Sheinbaum, J., Pallàs-Sanz, E., Tenreiro, M., Ochoa, J., Ruiz-Angulo, A., ... & de Marez,
1074 C. (2020). Heat Content Anomaly and Decay of Warm-Core Rings: the Case of the Gulf of Mexico.
1075 *Geophysical Research Letters*, 47(3), e2019GL085600.
1076

1077 Meunier, T., Tenreiro, M., Pallàs-Sanz, E., Ochoa, J., Ruiz-Angulo, A., Portela, E., et al. (2018a).
1078 Intrathermocline eddies embedded within an anticyclonic vortex ring. *Geophysical Research Letters*,
1079 45. <https://doi.org/10.1029/2018GL077527>
1080

1081 Meunier, T., Pallàs-Sanz, E., Tenreiro, M., Rodriguez, E. P., Ochoa, J., Ruiz-Angulo, A., & Cusí, S.
1082 (2018b). The Vertical structure of a Loop Current Eddy. *Journal of Geophysical Research: Oceans*.
1083

1084 Mignot, A., Claustre, H., Uitz, J., Poteau, A., D'Ortenzio, F., and Xing, X., (2014), Understanding the
1085 seasonal dynamics of phytoplankton biomass and the deep chlorophyll maximum in oligotrophic
1086 environments: A Bio-Argo float investigation, *Global Biogeochem. Cy.*, 28, 856–876.
1087

1088 Monterey, G., & Levitus, S. (1997). Seasonal variability of mixed layer depth for the World Ocean
1089 (NOAA Atlas NESDIS 14, 100 p.). Silver Spring, MD: National Oceanic and Atmospheric
1090 Administration.
1091

1092 Muller-Karger, F. E., Walsh, J. J., Evans, R. H., & Meyers, M. B. (1991). On the seasonal
1093 phytoplankton concentration and sea surface temperature cycles of the Gulf of Mexico as determined
1094 by satellites. *Journal of Geophysical Research*, 96(C7), 12645–12665.
1095

1096 Myers, V. B., & Iverson, R. I. (1981). Phosphorus and nitrogen limited phytoplankton productivity in
1097 northeastern Gulf of Mexico coastal estuaries. In *Estuaries and nutrients* (pp. 569-582). Humana Press.
1098

1099 Nencioli, F., C. Dong, T. Dickey, L. Washburn, and J. C. McWilliams (2010), A vector geometry-
1100 based eddy detection algorithm and its application to a high-resolution numerical model product and
1101 high-frequency radar surface velocities in the Southern California Bight, *J. Atmos. Oceanic Technol.*,
1102 27, 564–579, doi:10.1175/2009JTECHO725.1.
1103

1104 Nof, D., 1981: On the b-induced movement of isolated baroclinic eddies. *J. Phys. Oceanogr.*, 11, 1662–
1105 1672, [https://doi.org/ 10.1175/1520-0485\(1981\)011,1662:OTIMOI.2.0.CO;2](https://doi.org/10.1175/1520-0485(1981)011,1662:OTIMOI.2.0.CO;2).
1106

1107 Nowlin, W. D. Jr., & Parker, C. A. (1974). Effects of a cold-air outbreak on shelf waters of the Gulf of
1108 Mexico. *Journal of Physical Oceanography*, 4(3), 467–486.

1109

1110 Omand, M. M., D'Asaro, E. A., Lee, C. M., Perry, M. J., Briggs, N., Cetinić, I., & Mahadevan, A.
1111 (2015). Eddy-driven subduction exports particulate organic carbon from the spring bloom. *Science*,
1112 348(6231), 222-225.

1113

1114 Omand, M. M., & Mahadevan, A. (2014). Shape of the oceanic nitracline. *Biogeosciences Discussions*,
1115 11, 14729–14763.

1116

1117 Oschlies, A., & Garçon, V. (1998). Eddy-induced enhancement of primary production in a model of the
1118 North Atlantic Ocean. *Nature*, 394(6690), 266.

1119

1120 Pallàs-Sanz, E., Candela, J., Sheinbaum, J., Ochoa, J., & Jouanno, J. (2016). Trapping of the near-
1121 inertial wave wakes of two consecutive hurricanes in the Loop Current. *Journal of Geophysical*
1122 *Research: Oceans*, 121(10), 7431-7454.

1123

1124 Passalacqua, G. A., Sheinbaum, J., & Martinez, J. A. (2016). Sea surface temperature influence on a
1125 winter cold front position and propagation: Air-sea interactions of the 'Nortes' winds in the Gulf of
1126 Mexico. *Atmospheric Science Letters*, 17(5), 302–307.

1127

1128 Polovina, J. J., Howell, E. A., & Abecassis, M. (2008). Ocean's least productive waters are expanding.
1129 *Geophysical Research Letters*, 35(3).

1130

1131 Sathyendranath, S, Brewin, RJW, Müeller, D, Brockmann, C, Deschamps, P-Y, Doerffer, R, Fomferra,
1132 N, Franz, BA, Grant, MG, Hu C, Krasemann, H, Lee, Z, Maritorea, S, Devred, E, Mélin, F, Peters, M,
1133 Smyth, T, Steinmetz, F, Swinton, J, Werdell, J, Regner, P (2012) Ocean Colour Climate Change

1134 Initiative: Approach and Initial Results, IGARSS 2012, 2024-2027.

1135 doi:10.1109/IGARSS.2012.6350979.

1136

1137 Sheinbaum Pardo, J., Athie De Velasco, G. E., Candela Perez, J., Ochoa de la Torre, J. L., & Romero
1138 Arteaga, A. M. (2016). Structure and variability of the Yucatan and loop currents along the slope and
1139 shelf break of the Yucatan channel and Campeche bank. *Dynamics of Atmospheres and Oceans*, 76,
1140 217–239. <https://doi.org/10.1016/j.dynatmoce.2016.08.001>

1141

1142 Sherr, E. B., & Sherr, B. F. (2002). Significance of predation by protists in aquatic microbial food
1143 webs. *Antonie van Leeuwenhoek*, 81(1), 293-308.

1144

1145 Siegel, D. A., Behrenfeld, M. J., Maritorena, S., McClain, C. R., Antoine, D., Bailey, S. W., ... & Eplee
1146 Jr, R. E. (2013). Regional to global assessments of phytoplankton dynamics from the SeaWiFS
1147 mission. *Remote Sensing of Environment*, 135, 77-91.

1148

1149 Siegel, D. A., McGillicuddy Jr, D. J., & Fields, E. A. (1999). Mesoscale eddies, satellite altimetry, and
1150 new production in the Sargasso Sea. *Journal of Geophysical Research: Oceans*, 104(C6), 13359-
1151 13379.

1152

1153 Sosa-Gutiérrez, R., et al. "Erosion of the Subsurface Salinity Maximum of the Loop Current Eddies
1154 From Glider Observations and a Numerical Model." *Journal of Geophysical Research: Oceans* 125.7
1155 (2020): e2019JC015397.

1156

1157 Strickland, J. D. H. (1965). Production of organic matter in the primary stages of the marine food
1158 chain, *Chem. Oceanogr.*, 1, 477–610.

1159

1160 Sturges, W., & Leben, R. (2000). Frequency of ring separations from the Loop Current in the Gulf of
1161 Mexico: A revised estimate. *Journal of Physical Oceanography*, 30, 1814–1819.

1162

1163 Sturges, W., & Kenyon, K. E. (2008). Mean flow in the Gulf of Mexico. *Journal of Physical*
1164 *Oceanography*, 38(7), 1501-1514.

1165

1166 Sweeney, E. N., D. J. McGillicuddy, and K. O. Buesseler (2003), Biogeochemical impacts due to
1167 mesoscale eddy activity in the Sargasso Sea as measured at the Bermuda Atlantic Time-series Study
1168 (BATS), *Deep Sea Res., Part II*, 50(22–26), 3017–3039, doi:10.1016/j.dsr2.2003.07.008.

1169

1170 Tenreiro, M., Candela, J., Sanz, E. P., Sheinbaum, J., & Ochoa, J. (2018). Near-Surface and Deep
1171 Circulation Coupling in the Western Gulf of Mexico. *Journal of Physical Oceanography*, 48(1), 145-
1172 161.

1173

1174 Travis, S., & Qiu, B. (2020). Seasonal Reversal of the Near-Surface Chlorophyll Response to the
1175 Presence of Mesoscale Eddies in the South Pacific Subtropical Countercurrent. *Journal of Geophysical*
1176 *Research: Oceans*, 125(3), e2019JC015752.

1177

1178 Turner, J. S. (1973). *Buoyancy effects in fluids* (368 p.). New York, NY: Cambridge University Press.

1179

1180 Turner, R. E., Rabalais, N. N., & Justic, D. (2006). Predicting summer hypoxia in the northern Gulf of
1181 Mexico: Riverine N, P, and Si loading. *Marine pollution bulletin*, 52(2), 139-148.

1182

1183 Vukovich, F. M., 2007: Climatology of ocean features in the Gulf of Mexico using satellite remote
1184 sensing data. *J. Phys. Oceanogr.*, 37, 689–707, <https://doi.org/10.1175/JPO2989.1>.
1185

1186 Waite, A. M., S. Pesant, D. A. Griffin, P. A. Thompson, and C. M. Holl (2007), *Oceanography*,
1187 primary production and dissolved inorganic nitrogen uptake in two Leeuwin Current eddies, *Deep Sea*
1188 *Res., Part II*, 54(8–10), 981–1002, doi:10.1016/j.dsr2.2007.03.001.
1189

1190 Wawrik, B., Paul, J., Bronk, D., John, D., Gray, M., 2004. High rates of ammonium recycling drive
1191 phytoplankton productivity in the offshore Mississippi River plume. *Aquat. Microb. Ecol.* 35, 175–184.
1192 <http://dx.doi.org/10.3354/ame035175>.
1193

1194 Weisberg, R. H., & Liu, Y. (2017). On the Loop Current penetration into the Gulf of Mexico. *Journal*
1195 *of Geophysical Research: Oceans*, 122(12), 9679-9694.
1196

1197 Williams, R. G. (1988). Modification of ocean eddies by air-sea interaction. *Journal of Geophysical*
1198 *Research: Oceans*, 93(C12), 15523-15533.
1199

1200 Wu, G. (1964). Stratification and circulation in the Antillean-Caribbean basins (Vol. 1). New York,
1201 NY: Columbia University Press.
1202

1203 Zhao, J., Bower, A., Yang, J., & Lin, X. (2018). Meridional heat transport variability induced by
1204 mesoscale processes in the subpolar North Atlantic. *Nature communications*, 9(1), 1124.
1205

1206 Zhong, Y., & Bracco, A. (2013). Submesoscale impacts on horizontal and vertical transport in the Gulf
1207 of Mexico, *Journal of Geophysical Research: Oceans*, 118(10), 5651-5668.